A Simple Multiscale Intermediate Coupled Stochastic Model for El Niño Diversity and Complexity

Nan Chen[1] **and Xianghui Fang**[2,3,4]

[1]Department of Mathematics, University of Wisconsin-Madison, 480 Lincoln Drive, Madison, WI 53705, USA
[2]Department of Atmospheric and Oceanic Sciences and Institute of Atmospheric Sciences, Fudan University, 220 Handan Rd., Shanghai, 200433, China
[3]Innovation Center of Ocean and Atmosphere System, Zhuhai Fudan Innovation Research Institute, Zhuhai, 518057, China
[4]Shanghai Frontiers Science Center of Atmosphere-Ocean Interaction, Shanghai 200438, China

Key Points:

- The strength, occurrence frequency and spatiotemporal patterns of both the EP and the CP events are realistically reproduced.
- Strongly non-Gaussian statistics, seasonal phase locking and power spectrum are accurately recovered in all Niño 3, 3.4 and 4 regions.
- Both the composites of the SST anomalies and the strength-location bivariate distribution of SST maxima highly resemble the observations.

Corresponding author: Xianghui Fang, fangxh@fudan.edu.cn

Abstract

El Niño-Southern Oscillation (ENSO) is the most prominent interannual climate variability in the tropics and exhibits diverse features in spatiotemporal patterns. This paper develops a simple multiscale intermediate coupled stochastic model to capture the ENSO diversity and complexity. The model starts with a deterministic and linear coupled interannual atmosphere, ocean, and sea surface temperature (SST) system. It can generate two dominant linear solutions representing the eastern Pacific (EP) and the central Pacific (CP) El Niños, respectively. In addition to adopting a stochastic model for characterizing the intraseasonal wind bursts, another simple stochastic process is developed to describe the decadal variation of the background Walker circulation. The latter links the two dominant modes in a simple nonlinear fashion and advances the modulation of the strength and occurrence frequency of the EP and the CP events. Finally, cubic nonlinear damping is adopted to parameterize the relationship between subsurface temperatures and thermocline depth. The model succeeds in reproducing the spatiotemporal dynamical evolution of different types of ENSO events. It also accurately recovers the strongly non-Gaussian probability density function, the seasonal phase locking, the power spectrum, and the temporal autocorrelation function of the SST anomalies in all the three Niño regions (3, 3.4 and 4) across the equatorial Pacific. Furthermore, both the composites of the SST anomalies for various ENSO events and the strength-location bivariate distribution of equatorial Pacific SST maxima for the El Niño events from the model simulation highly resemble those from the observations.

Plain Language Summary

El Niño-Southern Oscillation (ENSO) is the most prominent interannual climate variability in the tropics and exhibits diverse spatiotemporal characteristics. Developing a dynamical model with intermediate complexity to simulate the ENSO diversity and complexity facilitates the understanding and predicting of the ENSO and the global climate. To this end, a multiscale model is developed here. It starts with a coupled linear and deterministic interannual atmosphere, ocean, and sea surface temperature (SST) system. Then suitable stochastic processes, nonlinearity, and seasonal synchronization are incorporated, connecting the interannual components with the intraseasonal wind bursts and the decadal variation of the background Walker circulation. The model can simulate different eastern and central Pacific ENSO events with realistic spatiotemporal patterns, strength, and frequency. It also accurately recovers the strongly non-Gaussian probability density function, the seasonal phase locking, the power spectrum, and the temporal autocorrelation function of the SST anomalies in all the three Niño regions (3, 3.4 and 4) across the equatorial Pacific. Furthermore, both the composites of the SST anomalies for various ENSO events and the strength-location bivariate distribution of equatorial Pacific SST maxima for the El Niño events from the model simulation highly resemble those from the observations.

1 Introduction

El Niño-Southern Oscillation (ENSO) is the most prominent interannual variability in the tropics. It also affects the global climate, ecosystem, and socioeconomic development through atmospheric teleconnections (Ropelewski & Halpert, 1987; McPhaden et al., 2006). Therefore, understanding and predicting ENSO is a central problem with significant societal impacts. Bjerknes (1969) first suggested that ENSO is the product of tropical air-sea interaction. Since then, considerable achievements have been made in its simulation and prediction abilities (Latif et al., 1998; Neelin et al., 1998).

From the traditional point of view, El Niño is defined as the anomalous warm sea surface temperature (SST) in the equatorial eastern Pacific (EP) region. Zebiak and Cane (1987) developed the first coupled ocean-atmosphere model of intermediate complexity that successfully characterizes and predicts these EP warming events. Several deterministic and linear conceptual models were also proposed to explain the slow physics of ENSO. Among

these models, the delayed oscillator (Schopf & Suarez, 1988) describes the delayed effects of oceanic wave reflection at the ocean's western boundary on the EP SST anomalies. In contrast, the recharge-discharge oscillator (F.-F. Jin, 1997a) combines SST dynamics and ocean adjustment dynamics into a coupled basinwide recharge oscillator that relies on the non-equilibrium between the zonal mean equatorial thermocline depth and wind stress.

With the continuously improved understanding of nature, the spatiotemporal diversity and complexity of the ENSO have been progressively highlighted (Capotondi et al., 2015; Timmermann et al., 2018). In particular, the observational data shows that the center of anomalous SST is mainly located in the EP from 1980 to 2000. In contrast, it lies more towards the central Pacific (CP) after 2000 (Ashok et al., 2007; Kao & Yu, 2009; Kim et al., 2012). See Panel (b) of Figure 1. The emergence of these different ENSO events is called the El Niño diversity (Capotondi et al., 2015). It suggests the existence of at least two types of El Niños, which are named the EP and the CP El Niños, when the peak of the SST anomaly locates in the cold tongue and near the dateline region, respectively (Larkin & Harrison, 2005; Yu & Kao, 2007; Ashok et al., 2007; Kao & Yu, 2009; Kug et al., 2009). It is essential to notice that the shift of the warming center can cause significant differences in the air-sea coupling over the equatorial Pacific, which changes the way ENSO affects the global climate and brings severe challenges to its prediction (D. Chen & Cane, 2008; E. K. Jin et al., 2008; Barnston et al., 2012; Z.-Z. Hu et al., 2012; Zheng et al., 2014; Fang et al., 2015; Sohn et al., 2016; Santoso et al., 2019). In addition to these two major categories, individual ENSO events further exhibit diverse characteristics in spatial pattern, peak intensity, and temporal evolution, known as the ENSO complexity (Timmermann et al., 2018). Thus, developing effective dynamical models that capture the ENSO complexity is of practical importance, not only for improving the understanding of the formation mechanisms of ENSO but advancing the prediction of different ENSO events and the associated varying climatic impacts as well.

The main physical mechanisms of the EP and the CP El Niños are very different. Due to the strong zonal asymmetry of the tropical Pacific air-sea system, the thermocline, a thin layer that separates the upper warm water from the cold water in the lower layer, is deep in the western Pacific (WP) while shallow in the EP region. Such a structure is consistent with the easterly trade wind. As a result, the SST in the EP is more susceptible to the oceanic vertical processes, i.e., the thermocline feedback. On the other hand, the background mean state suggests that the CP is the region with the most significant zonal SST gradient. Consequently, the anomalous zonal current can significantly affect the local SST variations, which means the development of the CP type of ENSO is primarily influenced by the zonal advective feedback (Kug et al., 2009, 2010; Ham & Kug, 2012; Kug et al., 2012; N. Chen & Majda, 2016; Fang & Mu, 2018; Fang & Zheng, 2018). It is worthwhile to point out that, since the state-of-the-art coupled general circulation models (CGCMs) in general have difficulties in accurately describing the mean state of the tropical Pacific (e.g., the unrealistic westward extension of the cold tongue), the simulations often contain biases in reproducing the equatorial SST gradient and the relevant zonal advective feedback (Lin, 2007; Fang & Zheng, 2018; Xie & Jin, 2018; Planton et al., 2021). Such an issue is one of the main reasons that result in significant challenges for the CGCMs to simulate the El Niño diversity correctly (Wittenberg, 2009; Ham & Kug, 2012; Capotondi et al., 2015).

In addition to the interannual state variables, it is essential to consider several other vital variabilities belonging to different temporal scales in the modeling procedure to generate the ENSO complexity realistically. On the one hand, the intraseasonal atmospheric variability, e.g., the westerly wind burst (WWB) (Harrison & Vecchi, 1997; Vecchi & Harrison, 2000; Tziperman & Yu, 2007) and the Madden-Julian oscillation (MJO) (Hendon et al., 2007; Puy et al., 2016), has been understood as one of the primary sources that lead to the ENSO irregularity and extreme events. Specifically, WWBs can influence ENSO development by stimulating eastward-propagating oceanic Kelvin waves, generating surface zonal currents, and weakening evaporation. Many modeling works have been attempted to incorporate semistochastic parameterization for the WWBs (Gebbie et al., 2007; Tziperman & Yu,

2007; Gebbie & Tziperman, 2009; Levine et al., 2016; Thual et al., 2016, 2017) and suggest that the coupled feedbacks between the interannual SST and the intraseasonal WWBs is sufficient to transfer a damped system to a semi-regular self-sustained oscillator. Likewise, in light of an intermediate coupled model (ICM), Lian et al. (2014) found that the WWBs are responsible for the existence of the irregularity and intensity of El Niño. The associated specific characteristics depend on the timing of the WWBs relative to the phase of the recharge–discharge cycle. On the other hand, ENSO is also modulated by the decadal variation of the background mean state. Notably, McPhaden et al. (2011) and Xiang et al. (2013) revealed the changes in the equatorial Pacific around the 2000s, i.e., a La Niña-like background state with enhanced trade winds and a more tilted thermocline, is in favor of the occurrence of more frequent CP El Niño events. This is consistent with the findings in Capotondi and Sardeshmukh (2015), which highlighted the importance of a La Niña-like initial/background state based on results from a linear inverse model. Power et al. (2021) also emphasizes the role of decadal variability in affecting the equatorial Pacific. In addition, by extending the original recharge oscillator into a three-region (i.e., WP, CP, and EP) conceptual model that contains a set of 6 stochastic ordinary differential equations and includes both the thermocline and zonal advective feedbacks, N. Chen et al. (2022) demonstrated that the decadal variability plays a crucial role in modulating the occurrence of the CP and EP El Niños.

The conceptual model in N. Chen et al. (2022) captures many desirable large-scale features of the ENSO complexity. It thus provides an essential theoretical basis for developing a more sophisticated dynamical model, namely an ICM, that aims to reproduce detailed spatiotemporal patterns of the ENSO complexity realistically. Unlike the conceptual models, the ICMs have the unique advantage of incorporating more elaborate underlying physics and spatially-extended dynamics into the model development that facilitate the understanding and prediction of nature. The ICMs also serve as a bridge that connects the low-order conceptual models and the more complicated CGCMs with a relatively low computational cost.

To this end, a stochastic ICM for the ENSO complexity is developed in this paper. The dynamical core of this new stochastic ICM is deterministic and linear, which involves a coupled interannual atmosphere, ocean, and SST system that drives the essential ENSO dynamics in a simple fashion. Here, the latent heating proportional to the SST is depleted from the ocean and forces an atmospheric circulation. In turn, the resulting zonal wind stress forces ocean dynamics that provide feedback to the SST through the thermocline depth anomalies and the ocean zonal advection. The coupled linear and deterministic interannual starting model can generate two dominant linear solutions representing the EP and the CP El Niños, respectively, which are essential for simulating the ENSO complexity. The interannual components are coupled with the intraseasonal and the decadal variabilities, described by suitable stochastic processes. The former is the main contributor to the ENSO irregularity and extreme events. At the same time, the latter links the two dominant modes in a simple nonlinear fashion and advances the modulation of the strength and occurrence frequency of the EP and the CP events. Seasonal synchronization is further incorporated into the model, facilitating the ENSO events to tend to peak in boreal winter. Finally, cubic nonlinear damping is adopted to parameterize the relationship between subsurface temperatures and thermocline depth. See Panel (a) of Figure 1 for a schematic illustration of the model structure and the key components. Note that the originally pioneering Zebiak and Cane (1987) ICM was not designed to characterize the ENSO complexity. A recently developed revised version captures certain diversity features of the ENSO (Geng & Jin, 2022). Nevertheless, the new simple ICM to be developed in this paper differs significantly from the Zebiak and Cane (1987) model and its revised version. The new model highlights the interactions between variabilities at different time scales, where only a minimum nonlinearity is adopted to maintain the model in a simple fashion. The model also exploits suitable stochastic processes to effectively characterize the dynamical properties and accurately reproduce the non-Gaussian statistics of the ENSO complexity in different Niño regions across

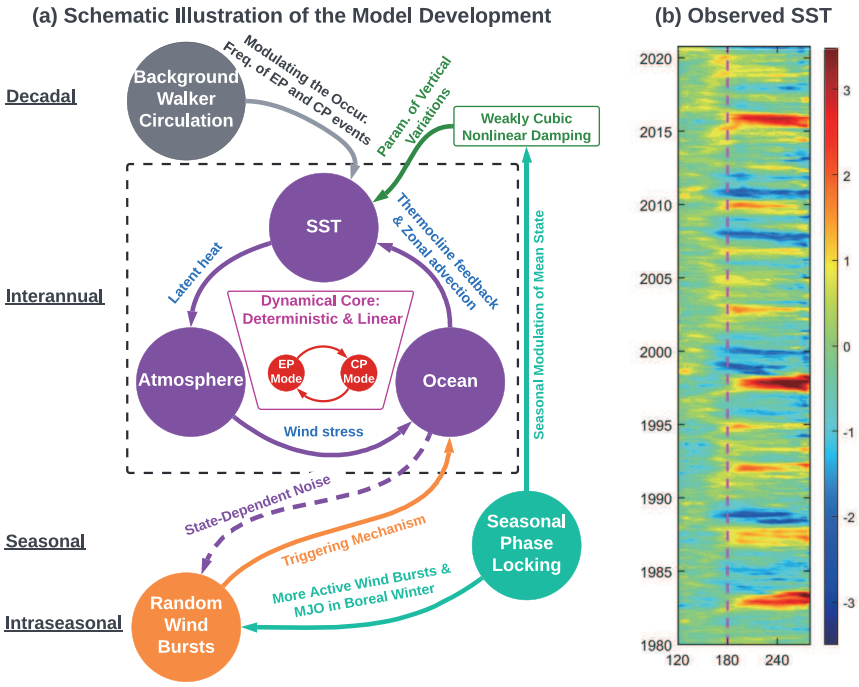

Figure 1. Panel (a): A schematic illustration of the multiscale model developed here. Panel (b): The observational SST anomaly from 1980 to 2020 (unit: ^{o}C). It is based on the GODAS dataset (Behringer & Xue, 2004) and is computed by averaging over 5^{o}S to 5^{o}N followed by removing the monthly mean climatology of the entire period.

the equatorial Pacific. The latter is particularly crucial to simulate various ENSO events realistically. It is an essential prerequisite for the unbiased statistical forecast of the ENSO complexity as well (Majda & Chen, 2018; Fang & Chen, 2022).

The rest of the paper is organized as follows. Section 2 presents the details of the simple stochastic ICM, including the deterministic and linear interannual components, the stochastic intraseasonal parameterization, the stochastic decadal process, the seasonal synchronization, and the nonlinearly coupled multiscale system. Section 3 contains the observational datasets and the definitions of different types of ENSO events. The model simulations are presented in Section 4 and are compared with the observations. In addition to showing the spatiotemporal patterns of different ENSO events, the skill of reproducing several key statistics in different Niño regions and the composite analysis are also highlighted in this section. Finally, Section 5 contains the conclusions and discussion.

2 The Simple Stochastic ICM

2.1 The starting deterministic and linear interannual model

The starting interannual model is a deterministic and linear coupled atmosphere-ocean-SST system:

Atmosphere:

$$\begin{aligned} &-yv-\partial_x\theta=0\\ &yu-\partial_y\theta=0\\ &-(\partial_x u+\partial_y v)=E_q/(1-\overline{Q}) \end{aligned} \tag{1}$$

Ocean:

$$\begin{aligned} &\partial_t U-c_1YV+c_1\partial_x H=c_1\tau_x\\ &YU+\partial_Y H=0\\ &\partial_t H+c_1(\partial_x U+\partial_Y V)=0 \end{aligned} \tag{2}$$

SST:

$$\partial_t T=-c_1\zeta E_q+c_1\eta_1 H+c_1\eta_2 U. \tag{3}$$

The coupled system (1)–(3) consists of a non-dissipative Matsuno–Gill type atmosphere model (Matsuno, 1966; Gill, 1980), a simple shallow-water ocean model (Vallis, 2016) and an SST budget equation (F.-F. Jin, 1997b). Here, the state variables u and v are the zonal and meridional wind speeds, θ is the potential temperature, U and V are the zonal and meridional ocean currents, H is the thermocline depth, and T is the SST. All of them are anomalies. For the coordinate variables, t is the interannual time coordinate, x is the zonal coordinate, while y and Y are the meridional coordinates for the atmosphere and ocean components, respectively. The reason for adopting two distinct meridional axes is that the atmosphere and ocean deformation radii are different. In these equations, $E_q=\alpha_q T$ is the latent heat with $\overline{Q}$ a constant representing the background vertical moisture gradient (Majda & Stechmann, 2009), $\tau_x=\gamma u$ is the wind stress, ζ is the latent heating exchange coefficient, η_1 and η_2 are the strengths of the thermocline and zonal advective feedback, respectively. Here, η_1 is stronger in the EP due to the shallower thermocline, while η_2 is stronger in the CP because of the more significant zonal gradient of the background SST in that region. The constant c_1 is related to the ratio between the ocean and atmosphere phase speeds. The atmosphere extends over the entire equatorial belt $0\le x\le L_A$ with periodic boundary conditions, namely $u(0,y,t)=u(L_A,y,t)$, and similar for other atmospheric variables. The Pacific Ocean extends over $0\le x\le L_O$ with reflection boundary conditions $\int_{-\infty}^{\infty}U(0,Y,t)\,\mathrm{d}Y=0$ and $U(L_O,Y,t)=0$ (Cane et al., 1981; F.-F. Jin, 1997b). The detailed parameter values are listed in Appendix.

The above model retains a few essential ingredients that couple the interannual atmosphere, ocean, and SST components and drive the critical ENSO dynamics in a simple fashion. Specifically, the latent heating E_q proportional to the SST T is removed from the ocean and forces an atmospheric circulation. The resulting zonal wind stress τ_x, in turn, forces ocean dynamics that provide feedback to the SST through the thermocline depth anomalies H and the zonal current U. See the dashed box in Panel (a) of Figure 1 that depicts the interannual components.

To facilitate the computation of the model solution, a meridional projection and truncation are applied to the coupled system, which is known to have meridional basis functions in the form of parabolic cylinder functions (Majda, 2003; Thual et al., 2016). To develop a simple ICM, only the leading basis function is kept for the atmosphere and the ocean, denoted by $\phi_0(y)$ and $\psi_0(Y)$, respectively. Both $\phi_0(y)$ and $\psi_0(Y)$ have Gaussian profiles and are centered at the equator, but the meridional span of $\phi_0(y)$ is more significant than that of $\psi_0(Y)$. The details of these basis functions are included in Appendix. The meridional truncations trigger atmosphere Kelvin, Rossby waves K_A, R_A, and ocean Kelvin, Rossby waves K_O, R_O. Once the system (1)–(3) is projected to the leading meridional basis functions, the dependence of y and Y are eliminated. The resulting system is only a function of t and x. It reads:

Atmosphere:

$$\begin{aligned} &\partial_x K_A = -\chi_A E_q (2-2\bar{Q})^{-1} \\ &-\partial_x R_A/3 = -\chi_A E_q (3-3\bar{Q})^{-1} \\ (B.C.)\quad &K_A(0,t) = K_A(L_A,t) \\ (B.C.)\quad &R_A(0,t) = R_A(L_A,t) \end{aligned} \tag{4}$$

Ocean:

$$\begin{aligned} &\partial_t K_O + c_1 \partial_x K_O = \chi_O c_1 \tau_x/2 \\ &\partial_t R_O - (c_1/3)\partial_x R_O = -\chi_O c_1 \tau_x/3 \\ (B.C.)\quad &K_O(0,t) = r_W R_O(0,t) \\ (B.C.)\quad &R_O(L_O,t) = r_E K_O(L_O,t) \end{aligned} \tag{5}$$

SST:

$$\partial_t T = -c_1 \zeta E_q + c_1 \eta_1 (K_O + R_O) + c_1 \eta_2 (K_O - R_O), \tag{6}$$

where r_W and r_E are the reflection coefficients associated with the ocean reflection boundary conditions (B.C.). The constants χ_A and χ_O are the meridional projection coefficients with $\chi_A = \int_{-\infty}^{\infty} \phi_0(y)\phi_0(y/\sqrt{c})dy$ and $\chi_O = \int_{-\infty}^{\infty} \psi_0(Y)\psi_0(\sqrt{c}Y)dY$. Once these waves are solved, the physical variables can be reconstructed,

$$\begin{aligned} u &= (K_A - R_A)\phi_0 + (R_A/\sqrt{2})\phi_2 \\ \theta &= -(K_A + R_A)\phi_0 - (R_A/\sqrt{2})\phi_2 \\ U &= (K_O - R_O)\psi_0 + (R_O/\sqrt{2})\psi_2 \\ H &= (K_O + R_O)\psi_0 + (R_O/\sqrt{2})\psi_2 \end{aligned} \tag{7}$$

where ϕ_2 and ψ_2 are the third meridional bases of atmosphere and ocean, respectively. Note that T, τ and E_q in (4)–(6) stand for the variables after the meridional projection. Despite adopting the same notation, they differ from the original variables in (1)–(3). In addition, the reflection coefficients r_W and r_E are calculated by using the boundary conditions: $\int_{-\infty}^{\infty} U(0,Y,t)dY = 0$ at the western boundary and $U(L_O,Y,t) = 0$ at the eastern boundary. The former integrates U in (7) and gives $r_W = 0.5$. The latter implies U is zero at different latitude points. In other words, it requires the projected velocity field to each meridional basis function to be zero. Thus, the velocity projected to the leading basis ψ_0 leads to $K_O = R_O$ or $r_E = 1$. It is also worth remarking that the equations (4)–(6) are projected only to the leading meridional basis function while the reconstruction in (7) also includes the third one. This is due to the use of the so-called raising and lowering operators in deriving the truncated equations, which connect the nearby meridional basis functions. See Majda (2003); Biello and Majda (2006); Stechmann and Majda (2015) for more technical details. It is worth remarking that the higher order meridional basis functions would include off-equatorial contributions to the equatorial dynamics, which could be essential to account for the negative feedback associated with off-equatorial Rossby waves (Kirtman, 1997; Capotondi et al., 2006) or the effect of off-equatorial influences, for example, the north and south Pacific meridional modes (Chiang & Vimont, 2004; Zhang et al., 2014). Nevertheless, this work aims to develop a simple ICM that characterizes explicit physics at the leading order. The stochastic noise can effectively describe certain statistical feedback from the off-equatorial regions.

After applying a spatial discretization in the x direction, the coupled system (4)–(6) is solved numerically via an upwind finite difference scheme. Since the coupled system is linear and deterministic, its final solution, after the numerical discretization is applied, can be written as a superposition of a set of non-interacting linear modes (the so-called linear solutions). Each linear solution is associated with one eigenmode of the system. In the numerical discretization here, the entire equatorial band is divided into N_A equidistance

grids, and there are N_O grid points in the Pacific ocean. In the simulations of this paper, $N_A = 128$ and $N_O = 56$ are utilized. In other words, the distance between every two grid points is 312.5km, as the entire equatorial band and the span of the Pacific ocean are $40,000$km and $17,500$km, respectively. With an appropriate choice of physical parameters (see Appendix), all the eigenvalues have negative real parts, indicating the decaying nature of these linear solutions. It is essential to highlight that although the eigenvalues of the strongly decaying and fast oscillating small-scale modes may vary by changing the resolution in the spatial discretization, the leading two eigenmodes with the slowest decaying rate remain almost unchanged as long as the spatial discretization is not too coarse. The leading two eigenmodes appear as a pair, and the associated eigenvalues are complex and conjugate, where the associated oscillation frequency lies on the interannual time scale. Due to the slowest decaying rate, the full solution of the coupled system (4)–(6) is dominated by these eigenmodes (see Appendix for details).

Figure 2 shows the spatiotemporal evolution of the leading two eigenmodes. In this figure, the decaying rate is manually set to zero to demonstrate the spatiotemporal pattern of such linear solutions. By varying the strength of the zonal advective feedback coefficient η_2, the dominant eigenmodes can have distinct behavior (see Appendix for the exact parameter values). Specifically, if the role of the zonal advection is weakened, then the leading linear solution exhibits spatiotemporal patterns with the EP El Niño dominating. See Panel (a). In such a situation, the thermocline feedback is the primary mechanism for generating the EP events. In addition, the convergence center of the atmospheric wind lies in the eastern Pacific. On the other hand, if the zonal advective feedback becomes stronger, then the CP El Niño pattern becomes dominant. Correspondingly, the zonal ocean current leads to the warming in the CP region, and the associated convergence center of the atmospheric wind shifts westward. See Panel (b). In addition, the thermocline is deeper than average during the development phase of EP events and steeper than average (La Niña-like) during the development phase of CP events, as described in Capotondi and Sardeshmukh (2015). It is worth highlighting that the occurrence frequency of the CP events (every 2.5 years) is higher than that of the EP events (every 4.5 years) in these dominant linear solutions, which is consistent with the observations. Note that these two linear solutions are the necessary conditions and mechanisms for the model to capture the ENSO complexity.

It is worth mentioning that Fedorov and Philander (2001) suggested in their stability analysis the EP-like and CP-like linear modes feature eastward and westward SST propagation, respectively. This is slightly different from the results shown here. In Fedorov and Philander (2001), the mean state of the SST is calculated by a simple model with the specified mean thermocline depth (H) and the temperature difference across the thermocline ($\triangle T$). Note that this simple model is proper for the anomalous fields in the tropical Pacific but could be too crude to depict the mean state since the latter is much more complicated than the former. As a result, the reconstructed mean state of the SST is flat in the central Pacific, i.e., with nearly zero zonal gradients. Since the zonal SST gradient of the mean state directly determines the strength of the zonal advective feedback ($-u\bar{T}_x$), it is crucial for developing the CP type of ENSO event. To this end, a more refined structure function η_2 is adopted here to represent the strength of the zonal advective feedback (or the zonal SST gradient of the mean state), which shows a large center in the central Pacific region.

2.2 Simple stochastic models for the intraseasonal and decadal variabilities

As was seen in Section 2.1, the coupled system (4)–(6) can generate basic linear solutions that exhibit regular patterns of the EP and CP El Niño events in different situations. However, the irregularity and complexity of ENSO require extra mechanisms beyond the deterministic and linear dynamics. In particular, the ENSO variability is often triggered or inhibited by a broad range of random atmospheric disturbances in the tropics, such as the WWBs (Harrison & Vecchi, 1997; Vecchi & Harrison, 2000; Tziperman & Yu, 2007), the easterly wind bursts (EWBs) (S. Hu & Fedorov, 2016), as well as the convective envelope

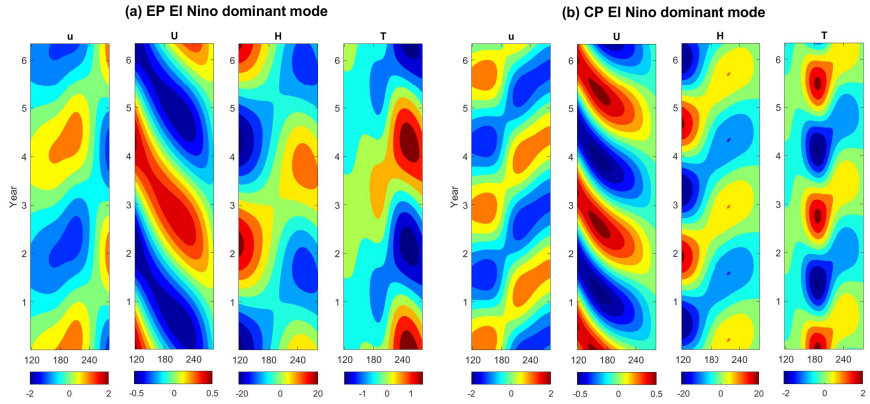

Figure 2. Linear solutions of the coupled system (4)–(6) reconstructed utilizing the leading two eigenmodes, which have the slowest decaying rate. These two modes appear as a pair of complex conjugate and therefore the reconstructed spatiotemporal pattern is real-valued. Panel (a) shows the solution by multiplying a small number to the ocean zonal advective feedback η_2 coefficient to lower its role and thus gives a EP El Niño dominant mode. Panel (b) shows the solution of the system with a stronger zonal advective feedback and leads to a CP El Niño dominant mode. In both panels, the four columns present the hovmoller diagrams of the interannual atmosphere wind u (unit: m/s), the ocean current U (unit: m/s), the thermocline depth H (unit: m) and the SST T (unit: ^{o}C). The detailed parameter values corresponding to the results here are listed in Appendix. Note that, for the purpose of illustration, the decaying rate is manually set to be zero in demonstrating the spatiotemporal pattern of such linear solutions here.

of the MJO (Hendon et al., 2007). On the other hand, it has been shown that the EP and CP events were alternatively prevalent every 10 to 20 years over the past century (Yu & Kim, 2013; Dieppois et al., 2021). For example, the EP events were the dominant ones in the 1980s and 1990s, while the CP El Niños more frequently occurred after 2000 (D. Chen et al., 2015; Freund et al., 2019). These findings imply that the decadal variability plays a crucial role in driving the transitions between the CP- and EP-dominant regimes. Thus, it is also essential to incorporate the decadal effect into the coupled ENSO model to link the different linear solutions.

To this end, two stochastic processes are developed and coupled to the starting interannual model (4)–(6). These two stochastic processes characterize the intraseasonal random wind bursts and the decadal variability, respectively. The former is a natural component that depicts random atmospheric disturbances. The latter describes the decadal variation of the background Walker circulation. It may be related to the climate change scenario and plays a vital role in modulating the strength and the occurrence frequency of the EP and the CP events (D. Chen et al., 2015; N. Chen et al., 2022).

First, with the stochastic wind bursts, the wind stress τ_x now contains two components $\tau_x = \gamma(u + u_p)$, where u remains the same as the atmospheric circulation in (2) while u_p is the contribution from the stochastic wind bursts, which is assumed to have the following structure,

$$u_p(x, y, t) = a_p(t)s_p(x)\phi_0(y),$$

where $\phi_0(y)$ is again the leading meridional basis while $s_p(x)$ is a fixed spatial structure localized in the western Pacific because most of the observed wind bursts are active there (see Appendix). The time series $a_p(t)$ describes the wind burst amplitude and is governed

by a simple one-dimensional real-valued stochastic process (Gardiner, 2009)

$$\frac{\mathrm{d}a_p}{\mathrm{d}t} = -d_p a_p + \sigma_p(T_C)\dot{W}_p, \tag{8}$$

where d_p is the damping term chosen such that the decorrelation time of the wind is about one month. In (8), $\dot{W}_p$ is a white noise source while $\sigma_p(T_C)$ is its strength. When a_p is positive and negative, it represents the WWB and EWB, respectively. It is important to highlight that the noise strength $\sigma_p(T_C)$ is state-dependent (the so-called multiplicative noise), as a function of the interannual SST from (6) averaged over the western-central Pacific, namely Niño 4 region. In the absence of seasonal cycle and decadal influence, $\sigma_p(T_C) = 1.6(\tanh(T_C)+1)$. The reason for choosing such a state-dependent noise coefficient is that wind burst activity is usually more active with warmer SST in the western-central Pacific due to the strengthening or eastward extension of the warm pool (Vecchi & Harrison, 2000; Hendon et al., 2007), which is modeled here in a simple parameterized fashion. This also implies that the level of stochastic forcing is larger during El Niño than La Niña events (Capotondi et al., 2018). The choice of the hyperbolic tangent function guarantees the bounded wind strength even with a very strong SST, which is more realistic than using a linear function. Note that the enhanced SST only increases the amplitude of the wind bursts. In contrast, the individual wind burst event generated from the stochastic process in (8) does not prefer westerly or easterly. This allows an equal chance to create both the WWB and the EWB as individual events consistent with the observations. Due to the state-dependent noise coefficient, the modeling procedure here indicates that the intraseasonal wind bursts not only affect the interannual variability but are also modulated by the latter.

Next, the decadal variability is driven by another simple stochastic process,

$$\frac{\mathrm{d}I}{\mathrm{d}t} = -\lambda(I - m) + \sigma_I(I)\dot{W}_I, \tag{9}$$

where the damping λ is set to be 5 years^{-1} representing the decadal time scale. Similar to (8), $\sigma_I(I)$ and $\dot{W}_I$ here are the state-dependent noise strength and the white noise source. The reason for adopting a state-dependent noise coefficient, which is a function of I itself, is to allow the distribution of I to be non-Gaussian. In particular, the trade wind in the lower level of the Walker circulation in the decadal time scale is easterly, which means the sign of I should stay the same throughout time, and thus the distribution of I is non-Gaussian. This feature can be easily incorporated into the process of I with the state-dependent noise coefficient (Averina & Artemiev, 1988; Q. Yang et al., 2021). Based on the limited observational data and the theory of inferring the least unbiased maximum entropy solution for a distribution, a uniform distribution between $[0, 1]$ is adopted for I in this work. Here, a larger I corresponds to a stronger easterly trade wind. The details of the maximum entropy solution and the way to determine $\sigma_I(I)$ are included in the Appendix. Note that the decadal variability I also stands for the zonal SST difference between the WP and CP regions that directly determines the strength of the zonal advective feedback. It is the primary interaction between decadal and interannual variabilities in the coupled system. In fact, in Kang et al. (2020), a Walker circulation strength index is defined as the sea level pressure difference over the CP/EP region (160^oW-80^oW, 5^oS-5^oN) and the Indian Ocean/WP region (80^oE-160^oE, 5^oS-5^oN). The monthly zonal SST gradient between the WP and CP region is highly correlated with this Walker circulation strength index (correlation coefficient being around 0.85), suggesting significant air-sea interaction over the equatorial Pacific. Since the latter is more directly related to the zonal advective feedback strength over the CP region, the decadal variable mainly illustrates such a feature.

2.3 Seasonal synchronization

Seasonal phase locking is one of the remarkable features of ENSO, which manifests in the tendency of ENSO events to peak during boreal winter and is mainly related to the pronounced seasonal cycle of the mean state (Tziperman et al., 1997; Stein et al., 2014).

Seasonal synchronization is incorporated into the multiscale coupled model developed above through two simple parameterizations.

First, the climatological SST in the central-eastern Pacific warms in spring and cools in boreal fall. This is partly because of the seasonal motion of the Intertropical Convergence Zone (ITCZ), which also modulates the strength of the upwelling and horizontal advection processes that influence the evolution of the SST anomalies (Mitchell & Wallace, 1992). Since the cool (warm) SSTs corresponds to the decreased (increased) convective activity and upper cloud cover, a time-dependent damping term is incorporated into the system to describe such a seasonal variation (Thual et al., 2017). It mimics the cloud radiative feedback. Specifically, two sinusoidal functions are utilized for parameterizing the otherwise constant α_q, which appears as $E_q = \alpha_q T$ in (6). One sinusoidal function has a period of one year that naturally describes the seasonal cycle. The other sinusoidal function has a period of half a year that represents a semiannual contribution to the seasonally modulated variance, as was suggested by Stein et al. (2014).

Second, the increased wind burst activity in the western Pacific during the boreal winter as a direct response to the increased atmospheric intraseasonal variability, such as the MJO, is another primary contributor to the seasonal synchronization (Hendon et al., 2007; Seiki & Takayabu, 2007). Therefore, a sinusoidal function with a period of one year is utilized for parameterizing the seasonal variation of the wind burst strength coefficient σ_p in (8).

2.4 The nonlinearly coupled multiscale system

The coupled model developed so far is a linear model, despite the state-dependent noise. However, the linear nature of the model is insufficient in characterizing some of the key observed dynamical and statistical features of the ENSO complexity.

From the dynamical point of view, at least two major nonlinearities are expected to be added to the starting linear model. First, the decadal variability determines the strength of the zonal advective feedback. Therefore, it is natural to treat the modulation of the decadal variability on the ENSO dynamics as nonlinear, where the decadal variability plays the role of a multiplicative factor of the zonal advection coefficient. In other words, the decadal variability I is incorporated into the SST budget equation (6) and appears in front of the zonal advection coefficient,

$$\partial_t T = -c_1\zeta E_q + c_1\eta_1(K_O + R_O) + c_1 I\eta_2(K_O - R_O) + c_1\eta_2 c_2, \tag{10}$$

such that a quadratic nonlinearity is introduced from $I(K_O - R_O)$ as I and K_O, R_O are both state variables (recall from (7) that K_O and R_O are the linear combination of H and U). This nonlinearity represents the mechanism that strengthening the Walker circulation in the decadal time scale will trigger more CP events. It is crucial in simulating the correct occurrence frequencies of both the CP and the EP El Niños. One additional small constant c_2 is added to (10), which guarantees all the variables have climatology with zero mean since otherwise, the nonlinearity can cause a slight shift of the mean state.

Another nonlinearity incorporated here is the damping coefficient in the SST equation. Recall that $E_q = \alpha_q T$ and therefore $-c_1\zeta\alpha_q$ is the damping coefficient. Here α_q is parameterized by a nonlinear quadratic function of the CP SST, and the spatial structure of such a nonlinear function is concentrated in the CP area. In addition, the symmetric axis of this quadratic function has a negative value, which means a stronger damping is imposed when the CP SST is positive. This effectively gives a cubic damping in the CP. The reason for introducing this nonlinearity is twofold. On the one hand, the relationship between the subsurface temperatures and the thermocline depth is more complicated in the CP region (Zhao et al., 2021). At the same time, only a simple shallow water model is utilized here. Thus, such nonlinear damping is introduced to parameterize the additional relationship beyond the capability of the shallow water model. On the other hand, it is justified from a simple statistical analysis of the observational data that a linear relationship between the

damping and SST anomaly in the CP region is broken. In contrast, a cubic nonlinearity fits the data in a more accurate fashion (N. Chen et al., 2022). The nonzero symmetric axis in parameterizing α_q is also crucial for recovering the correct non-Gaussian statistics of the SST in the CP region.

3 Observational Data Sets and the Definitions of Different Types of the ENSO Events

3.1 Data

The monthly SST data is taken from the GODAS dataset (Behringer & Xue, 2004). Anomalies are calculated by removing the monthly mean climatology of the entire period. The Niño 4, Niño 3.4, and Niño 3 indices are the average SST anomalies over the zonal regions 160^oE-150^oW, 170^oW-120^oW and 150^oW-90^oW, respectively, together with a meridional average over 5^oS-5^oN.

3.2 Definitions of different types of the ENSO events

The definitions of different El Niño and La Niña events for studying the ENSO complexity follow those in Kug et al. (2009), which are based on the average SST anomalies during boreal winter (December–January–February; DJF). When the EP is warmer than the CP, and the EP SST is more significant than 0.5^oC, it is classified as the EP El Niño. Among this, based on the definitions used by Wang et al. (2019), an extreme El Niño event corresponds to the situation that the maximum of EP SST anomaly from April to the following March is more significant than 2.5^oC. When the CP is warmer than the EP and larger than 0.5^oC, the event is defined as a CP El Niño. Finally, when either the CP or EP SST anomaly is cooler than -0.5^oC, it is defined as a La Niña event.

4 Model Simulation Results

The numerical solution of the model is calculated utilizing the forward Euler time integration scheme with a time step of 0.5 days for the interannual variabilities. The Euler-Maruyama scheme is adopted to compute the stochastic processes of the decadal variability and the intraseasonal wind bursts, with a numerical integration time step being 0.5 days and 0.05 days, respectively. The monthly averaged model outputs for the interannual and decadal variabilities are utilized in presenting the dynamical and statistical results. The monthly averaged output has almost no difference from the direct model solution but is adopted mainly to be consistent with the monthly averaged observational data. On the other hand, the monthly average is not applied to the wind burst data.

4.1 Model simulation of the ENSO complexity

Figure 3 shows a 50-year model simulation. With the random and nonlinear components in the model, the resulting atmosphere-ocean-SST fields exhibit irregular spatiotemporal patterns, mimicking the observed ENSO complexity (Panel (b) of Figure 1). To begin with, the model simulation succeeds in reproducing both the realistic CP (e.g., 154, 157, 160) and EP (e.g., 163, 175, 192) events as well as some mixed events (e.g., year 188). The two different linear solutions presented in Figure 2 are now linked by the decadal variability, which directly modulates the strength of the zonal advective feedback. In other words, the decadal variability preconditions the model to have a preference towards either the EP or the CP mode at each time instant, although the details of each single ENSO event are still primarily affected by other stochastic and nonlinear effects. Next, the spatiotemporal fields of the interannual atmosphere wind u, ocean current U, thermocline depth H, and the SST T in Panels (a)–(d), as well as the wind bursts strength a_p in Panel (f), reveal distinct formation mechanisms for the CP and EP El Niños. The EP El Niño, especially the extreme

EP El Niño, is triggered by the random wind bursts and the thermocline depth plays a vital role in the event development. In contrast, the zonal advection is the dominant contributor to the CP events. It is worth remarking that while the zonal advective feedback is the dominant dynamical feedback in the CP region, the development of anomalous zonal currents (for example, forced by anomalous winds) is also essential. A recent study (Capotondi & Ricciardulli, 2021) links the occurrence of CP events to extratropical wind precursors related to the North and South Pacific meridional modes. These off-equatorial wind anomalies can give rise to heat content anomalies in the CP region (Anderson et al., 2013) or lead to wind stress anomalies along the equator. The ICM developed here does not explicitly take into account the off-equatorial effects. But the stochastic effects may play a role in compensating for such effects. In addition to the response of the CP and EP events to the zonal advective and thermocline feedbacks, the convergence center of the interannual atmosphere wind locates in the CP and EP regions when these two types of events occur, respectively. These causal relationships are consistent with observations, and the previous findings (Kao & Yu, 2009; Kug et al., 2009; Xiang et al., 2013; Zheng et al., 2014; N. Chen et al., 2018). Furthermore, as in the observations, the strength of the CP El Niños is overall weaker than that of the EP ones (Zheng et al., 2014). Particularly, extreme El Niño events are only observed in the EP region due to the anomalously intense wind bursts. It is also noticed that the probability of generating CP events increases as the decadal variability becomes stronger. This is again consistent with the observations, for example, the CP events becoming more frequent as the strengthening of the Walker circulation in the 21st century (McPhaden et al., 2011; Xiang et al., 2013). Nevertheless, regardless of the strength of the decadal variability, the model always allows both the CP and the EP events to be triggered with a certain chance. Finally, the Niño indices shown in Panel (f) mimic reality, where the Niño 4 index has a slightly larger value than Niño 3 at the CP El Niño phases. In contrast, the Niño 3 index becomes much more significant than Niño 4 during extreme EP events.

Figure 4 shows a simulation of the SST field for 200 consecutive years, accompanied by the associated wind bursts and the decadal variability. To summarize the findings in these figures, Table 1 lists examples of different ENSO events belonging to 9 refined categories in such a long model simulation and are compared with observations. The results indicate the ability of the model to reproduce the realistic ENSO complexity. First, the model can simulate various EP El Niño events with different strengths. In addition to the moderate EP El Niños, the extreme El Niño events, which appear as a result of the strong WWBs generated from the intraseasonal model, are also reproduced by the model. It is worth highlighting that the so-called delayed super El Niño, as observed in 2014-2015 (S. Hu & Fedorov, 2016; Capotondi et al., 2018; Thual et al., 2019; Xie & Fang, 2020), are realistically simulated by the model, for example, during model years 905-906. The model succeeds in recovering the associated peculiar westerly-easterly-westerly wind burst structure that is the crucial mechanism to trigger such an El Niño event. Here, the initial WWB tends to start a strong El Niño, but the subsequent EWB kills the event and postpones it until the following year, when another series of strong WWBs occur. Next, the model generates many realistic CP El Niño events. In particular, both single-year (e.g., years 764 and 799) and multi-year (e.g., years 760-761 and 899-900) CP El Niño events can be reproduced from the model. The latter mimics the observed CP episodes, for example, during 2018-2020. In addition to those events that belong to either the EP or the CP categories, the model also creates some mixed CP-EP events (e.g., years 785 and 939), similar to the observed ones in the early 1990s (e.g., the one that occurred in the year 1992). Finally, the La Niña events from the model usually follow the El Niño ones as the consequence of the discharge phase. Some La Niña events have cold SST in the CP region, while others have cold centers around the EP area. The model can also simulate multi-year La Niña events. Namely, a La Niña transitioning to another La Niña, such as the one that spans over the years 774-775 and 902-904, mimicking the observed events 1999-2000 and 1984-1986, respectively. It is also worth pointing out that a few multi-year El Niño events (such as years 839-840, 918-919,

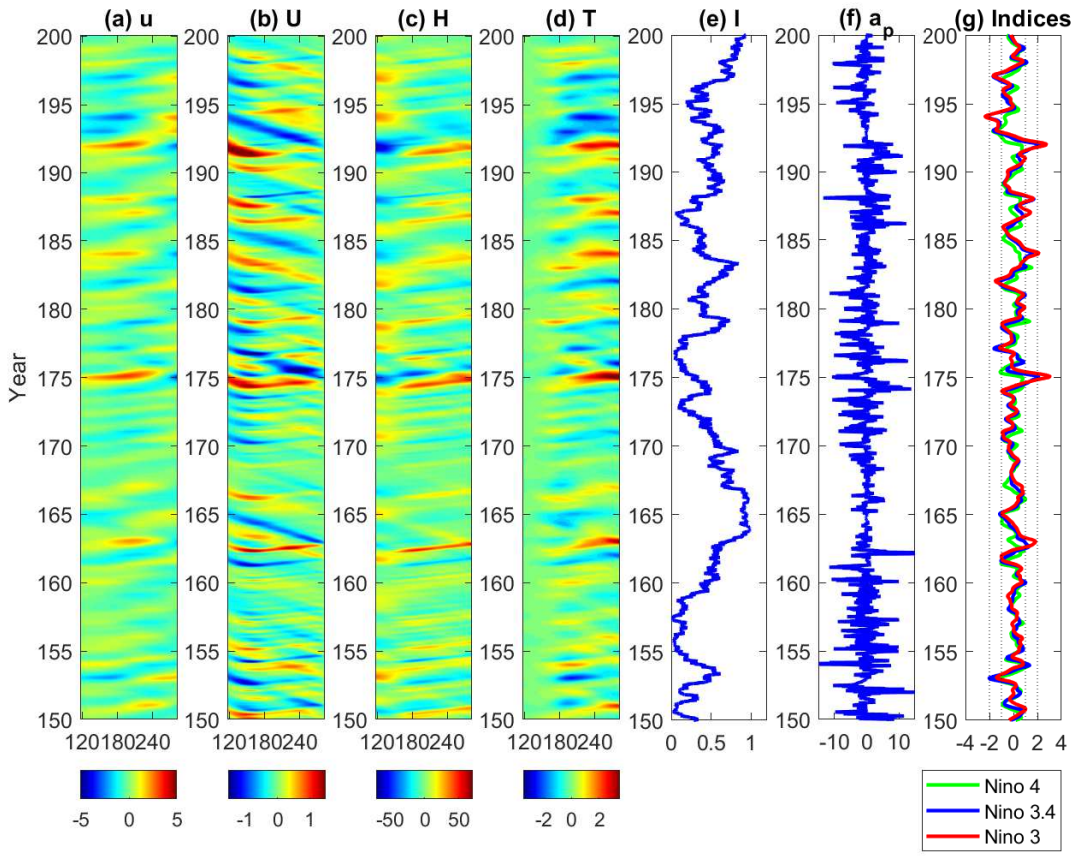

Figure 3. A 50-year model simulation of different fields. Panels (a)–(d): Hovmoller diagrams of the interannual atmospheric wind u (unit: m/s), the ocean current U (unit: m/s), the thermocline depth H (unit: m) and the SST T (unit: ^{o}C). The longitude ranges from 120^{o}E (120) to 80^{o}W (280). Panel (e): time series of the decadal variability I. Panel (f): time series of the intraseasonal random wind bursts a_p (unit: m/s). Panel (g): Niño 4, Niño 3.4 and Niño 3 indices.

Coarse category	Refined category	Model (yrs 750-950)	Observations (yrs 1980-2020)
EP El Niño			
	Moderate EP El Niño	792, 897	1987
	Super El Niño	752, 862	1998
	Delayed super El Niño	918-919, 905-906	2014-2015
CP El Niño			
	Single-year CP El Niño	764, 799	2005
	Multi-year CP El Niño:	760-761, 899-900	2018-2020
	CP La Niña	770, 848	1989
Mixed events			
	Mixed EP-CP El Niño	785, 939	1992
La Niña			
	Single-year La Niña	798, 802	2006
	Multi-year La Niña	774-775, 902-904	1999-2000

Table 1. Examples of different ENSO events in the model simulation (from year 750 to year 950; showing in Figure 4) and observations (from year 1980 to 2020). Here, two examples from the model simulation and one example from observations are listed for each type of the ENSO events, respectively.

935-936) in the model simulation are not directly found in observations. The randomly generated wind bursts mainly cause them.

4.2 Comparison of the statistics between model simulations and observations

In addition to the dynamical properties, the model statistics is another critical measurement for assessing its skill in reproducing realistic ENSO features. Since the focus is on the ENSO complexity, it is essential to study various statistics that represent unique aspects of the ENSO characteristics in different Niño regions across the equatorial Pacific. To this end, four statistical quantities concerning the SST anomalies of the model simulation are compared with those of the observations in Niño 4, Niño 3.4, and Niño 3 regions, respectively. They are 1) the probability density function (PDF), 2) the seasonal variance, 3) the power spectrum, and 4) the autocorrelation function (ACF). Here, the statistics of the observations are computed based on the observed SST between 1951 and 2020, which contains 70 years. On the other hand, a long simulation of 3500 years is utilized for computing the model statistics. The total simulation is divided into 50 non-overlapping subperiods, each having the same length as the observation. The statistics are then calculated for each of these 50 subperiods, the difference among which reflects the uncertainty in calculating these statistics.

Panel (a) of Figure 5 shows that the strong non-Gaussian statistics of the SST anomalies in all the three Niño regions are accurately recovered by the ICM developed here. In particular, the PDF of the Niño 3 SST from observations is highly skewed towards the positive direction with a one-sided fat tail. The tail corresponds to the occurrence of the extreme EP El Niños events. The state-dependent noise in the wind burst process facilitates the model to create such extreme events. Therefore, the model can accurately recover this strong non-Gaussian PDF. In contrast, a negative skewness is found in Niño 4 SST from observations. In addition, the kurtosis of the associated PDF is less than the standard Gaussian value, which is 3. These findings indicate the suppression of extreme El Niño events

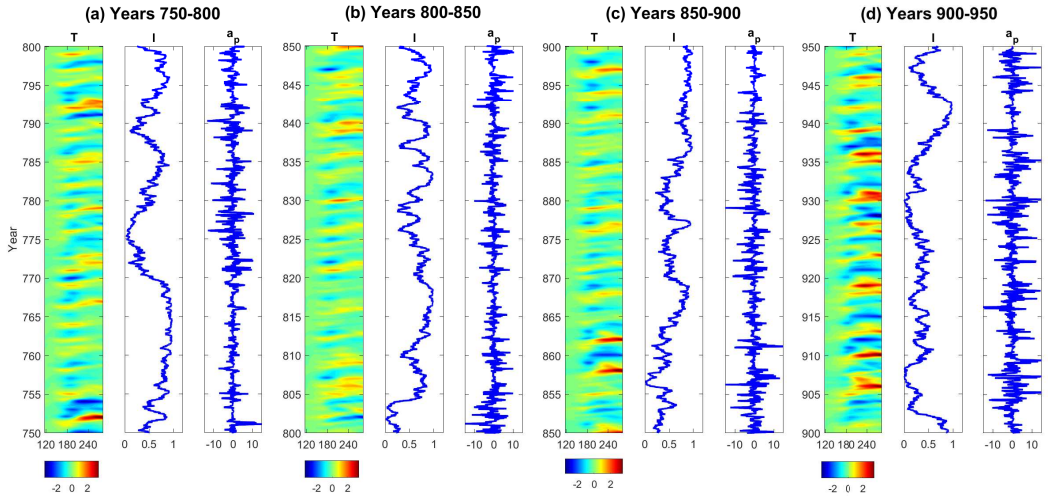

Figure 4. Model simulation: Hovmoller diagram of SST T (unit: ^{o}C), time series of the decadal variability I and time series of the intraseasonal random wind bursts a_p (unit: m/s) from year 750 to year 950.

in the Niño 4 region. With the help of the cubic and non-centered damping in the CP area, the model can accurately reproduce this skewed and light-tailed PDF. Similarly, the model can produce the observed PDF of the Niño 3.4 SST, demonstrating a slight positive skewness. It is worth highlighting that, despite the successes in recovering many dynamical features of ENSO, the CGCMs and many other dynamical models may not always be skillful in capturing such highly non-Gaussian PDFs in all the three Niño regions. However, recovering these statistics is one of the necessary conditions for reproducing the realistic ENSO complexity. Panel (b) of Figure 5 reveals the model's capability in recovering the observed seasonal synchronization of ENSO, which is represented by the monthly variance of the SST in different Niño regions. The observed ENSO events usually favor starting in spring and peaking in boreal winter. This will also be depicted in Figure 8 by the composite analysis for the temporal evolutions of Niño 3.4 SST index for different ENSO events. Overall, the model accurately captures these features, especially given that the model only exploits simple sinusoidal functions for parameterizing the seasonal effects.

Next, Panel (a) of Figure 6 shows the power spectrums of the SST. It can be seen that the significant signal of the power associated with the Niño 4 SST is between 2 and 4 years. The power decreases rapidly outside this window but another large power appears at lower frequencies, consistent with the presence of a decadal component associated with CP events (Sullivan et al., 2016). In contrast, the signal of the Niño 3 (and Niño 3.4) SST has a broader range in the interannual time scale; that is, the power remains significant between 2 and 7 years. All of these features, except the low frequency in the Niño 4 region, are well captured by the model simulations, which are the essential requirements for the model to generate a similar degree of irregularity in oscillations as in observations. In addition, as shown in Panel (b), although the ACF associated with the model decays slightly faster than the observations, the model can create very similar ACFs in different Niño 3.4 and Niño 4 regions as the observations. The results indicate that the model overall has a realistic decaying rate and memory, which are consistent with nature in the equatorial Pacific and are essential prerequisites for forecasting the ENSO complexity.

Finally, Figure 7 shows the scatter plot of the equatorial Pacific boreal winter (DJF) mean SST maxima for the El Niño events from the model simulation, which is compared with the observations. Each point displayed here is a function of the maximum SST and its

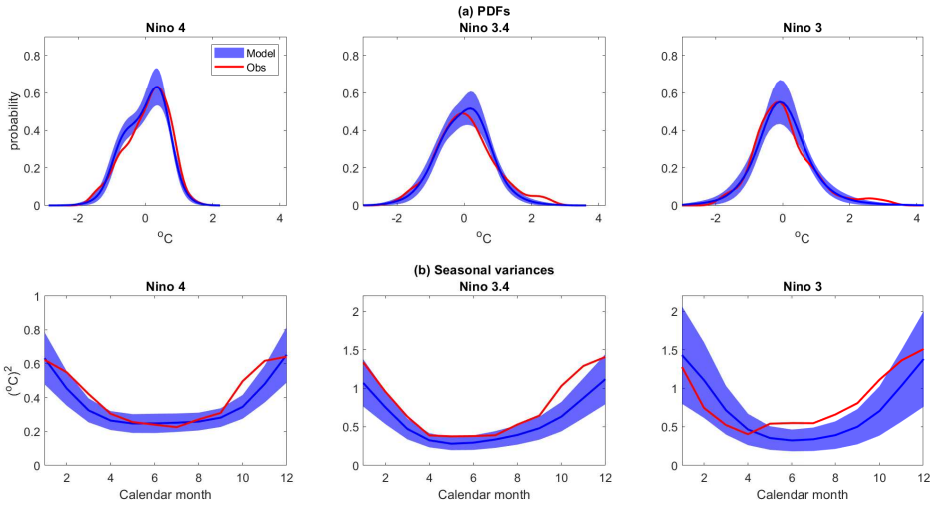

Figure 5. Comparison of the PDFs (Panel (a)) and the seasonal variances (Panel (b)) of SST anomalies between the model simulation and the observations in different Niño regions. The observations are based on the period of 1951-2020, which contains 70 years. Correspondingly, the model simulation has the length in total 3500 years and is divided into 50 equally long periods, each of which is 70 years. The blue shading area is the one standard deviation of the statistics computed from these 50 non-overlapped periods and the blue solid curve is the average value. The observational statistics is shown in red solid curve.

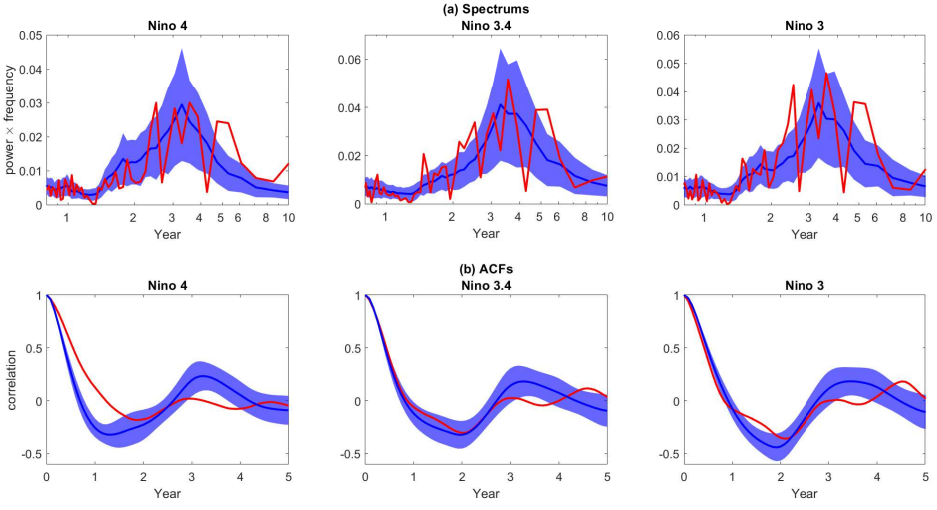

Figure 6. Similar to Figure 5 but for the spectrums (Panel (a)) and the autocorrelation functions (ACFs; Panel (b)).

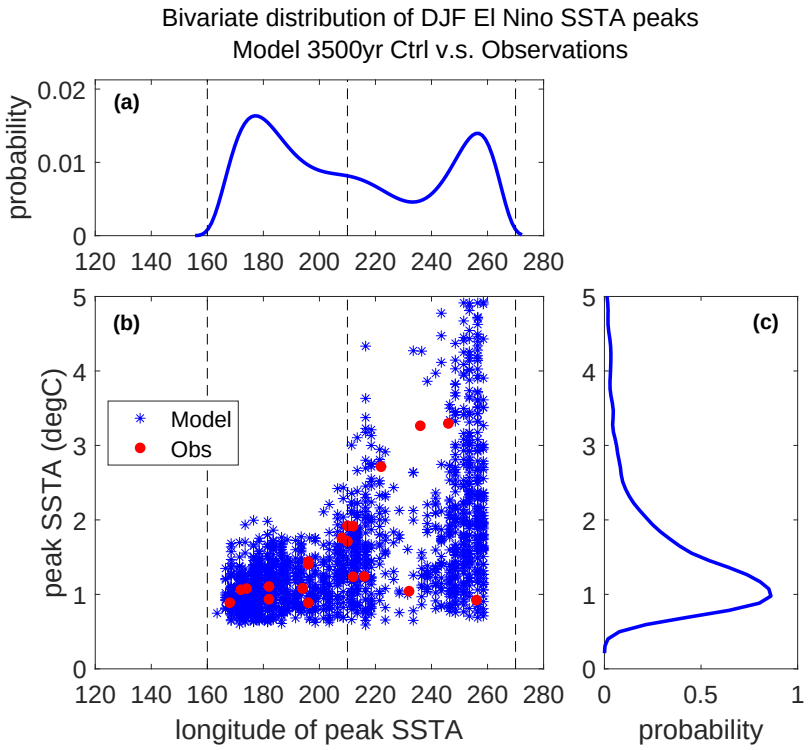

Figure 7. Distribution of equatorial Pacific SST maxima for the El Niño events from the model simulation of 3500 years (blue) and the observations (red). For each of the qualified El Niño events, the winter-mean SST anomalies are averaged over the equatorial zone (from 5^oS to 5^oN), and then the Pacific zonal maximum is located. (a) Distribution of peak SST anomaly longitudes. (b) Scatter plot of the peak SST anomaly value v.s. the longitude at which it occurs. The blue (red) dots are for the model results (observations). (c) Distribution of peak SST anomaly values.

corresponding longitude. Panel (a) shows the PDF of the locations of these El Niño events. It exhibits a bimodal distribution with two significant centers. One is near the dateline, and another is in the eastern Pacific. These two peaks correspond to the CP and EP El Niño events, respectively. The finding is consistent with those estimated from different observational data sets by Dieppois et al. (2021). The distribution from the simple ICM developed here is more accurate than those from many CGCM simulations. As was pointed out by Capotondi et al. (2020), many CGCM simulations have biases; for example, the CP events are often located too west compared with observations. Another desirable feature to highlight is that, despite the bimodality, there remains a relatively large probability of the event occurring in the region from the dateline to 120^oW (240). This reveals that ENSO diversity is not simply composed of events that belong to two separate categories. Instead, there are many mixed EP-CP events. In fact, according to Panel (b), there are several observed El Niño events (red dots) located in this region, indicating that the distribution should be in the form of a continuum rather than two disjoint sets (Johnson, 2013; Capotondi et al., 2015). However, this seems different in many CGCM results, as pointed out by Capotondi et al. (2015). Next, in terms of strength, the events with CP SST anomaly peaks are overall weaker than the corresponding EP ones. While the strongest events are always located in the eastern Pacific, the EP events can exhibit a wide range of amplitudes. These findings are consistent with physics and observations (F.-F. Jin et al., 2003).

	El Niño				La Niña	
	EP	CP	Extreme	Multi-year	Total	Multi-year
Obs	14	10	4	5	24	8
Model	18.2 ± 3.5	14.7 ± 3.5	3.1 ± 2.3	10.5 ± 1.6	26.1 ± 4.6	6.9 ± 2.6

Table 2. Occurrence frequency of different ENSO events per 70 years. The observations are based on the period of 1951-2020, which contains 70 years. For the model simulation, the mean value plus and minus one standard deviation computed from the 50 segments is shown for each case. Note that the counted number of the EP and the CP El Niños contains both single-year and multi-year events as well as the extreme events. Therefore, the total number of the El Niño events is simply the summation of the numbers in the first two columns (e.g., 24 in observations).

4.3 Composite analysis

To provide a more quantitative assessment of the model performance on simulating each type of the ENSO events, Table 2 summarizes the occurrence frequency of different El Niño and La Niña events (as defined in Section 3.2) per 70 years. For the El Niño events, although the occurrence frequency of both the CP and the EP El Niño events from the model (18.2 and 14.7) is higher than that from the observations (14 and 10), the gap in counting both types of the El Niños between the model and the observations is just around one standard deviation of different model simulation segments, which is nevertheless within a relatively reasonable range. Such a difference mainly comes from overestimating the number of the multi-year El Niño events in the model. Except for this overestimation issue, other statistics from the model simulation are similar to those from the observations. First, the ratio between the numbers of the EP and the CP El Niño events relative to the total number of events from the model simulation (55% v.s. 45%) is almost the same as that in the observations (58% v.s. 42%), which indicates the skill of the model in capturing the overall El Niño diversity. Second, four extreme El Niño events have occurred since 1951, namely 1972–1973, 1982–1983, 1997–1998, and 2015–2016, while a comparable number of 3.1 ± 2.3 events is found in the model simulations. Third, the occurrence frequency for the La Niña events (26.1 ± 4.6) from the model is very close to that in the observations (24). In particular, the model and the observations share approximately the same numbers of single-year and multi-year La Niña events. It is worthwhile to remark that, as the classification of El Niño events in observations is subject to the limited sample size and suffers from uncertainties associated with varying datasets (Wiedermann et al., 2016; Capotondi et al., 2020), the perfect agreement of the occurrence frequency with observations should not be a strict metric on evaluating the model performance. Therefore, it can be concluded that the model is skillful in reproducing reasonably accurate numbers of different events.

Next, Figure 8 exhibits the composites of the DJF mean SST anomalies on the equatorial Pacific for the EP El Niño, the CP El Niño, and the La Niña concerning the spatial distribution. Here, all the ENSO events (i.e., during the entire 3500 model years) are compared with the observations instead of separating them into smaller segments (see Panels a and b). It is seen that the composites computed from the model simulation are almost identical to those from the observations in terms of both the spatial patterns and the amplitudes. Specifically, the warming center locates in the EP and CP regions for the EP and CP El Niños, respectively, although the simulated EP events are closer to the coastline of South America. The cooling center of La Niña is located between the warming centers of the EP and CP El Niño, which is also in accordance with the observations. Next, the model succeeds in recovering the ENSO asymmetry. In other words, the amplitude of the EP El Niño is overall stronger than those of the CP El Niño, and the La Niña (Hayashi et al., 2020). It should be noticed that accurately reproducing the spatial distributions of the

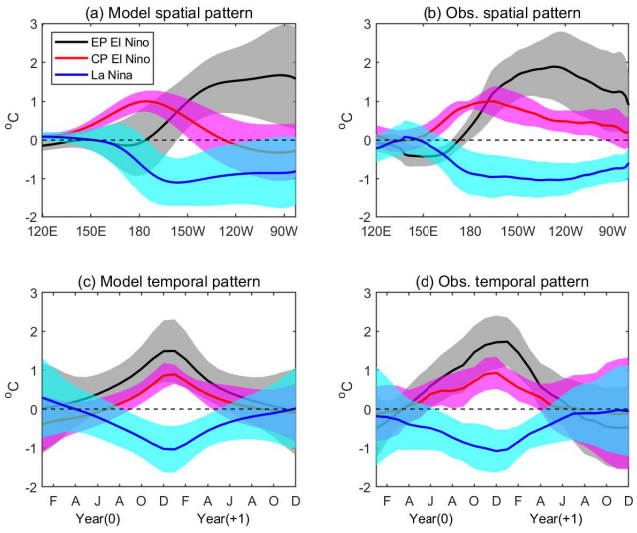

Figure 8. Upper panels: composited winter (DJF) mean SST anomalies (lines) and the corresponding error bars (i.e., shaded by one standard deviation) over the equatorial Pacific for EP El Niño (black), CP El Niño (red) and La Niña (blue) events. (a) and (b) are for model and observation, respectively. Lower panels: composited temporal evolution of the Niño 3.4 index for different types of ENSO events. Year(0) and Year(+1) represent the developing and decaying years of each event, respectively.

ENSO events and the ENSO asymmetry is still one of the main challenges for the state-of-the-art CGCMS (Planton et al., 2021). On the other hand, the model also realistically captures the composite results of temporal evolutions of the Niño 3.4 index for different types of ENSO events (see Panels c and d). Remarkably, they all show significant seasonal phase locking character, consistent with the discussion in Figure 5.

4.4 Sensitivity analysis

What remains is to study the role of each critical process in the coupled model, which facilitates understanding the model dynamics. To this end, several sensitivity tests are carried out in the following.

Let us begin by investigating the role of decadal variability. In the standard run, I is driven by a simple stochastic process (9), and its value of the decadal variability time series varies between 0 and 1. In the sensitivity tests, the model simulations with a fixed I of either $I \equiv 0$ or $I \equiv 1$ are studied. In each trial, the strength of the wind bursts is slightly tuned by multiplying a constant such that the variance of the SST remains the same as the standard run, which allows a fair comparison of the occurrence frequency in different scenarios. Note that the decadal variability may be related to climate change and climate projection. Therefore, the interannual variability response due to the decadal variability variation is of great interest. First, the decadal variability is set to be zero (i.e., $I \equiv 0$), which corresponds to the situation with a weakened background Walker circulation between 1980 and 2000 but towards the more extreme case. In such a scenario, the model simulation leads to an increase of the El Niño events (from 32.9 to 42.1 per 70 years) and a decrease of the La Niña ones (from 26.1 to 19.4). More specifically, among the El Niño events, 65.8% events are the EP type while only 34.2% events remain as the CP El Niño. This means the scenario with a weakened Walker circulation is more favorable for the EP than the CP

El Niño events, as the zonal advective feedback in this situation is reduced and the role played by the thermocline feedback becomes dominant. The CP El Niño events can still be generated because of the stochastic noise. Similar to the overall occurrence frequency, more multi-year El Niño (from 10.5 to 15.9) and less multi-year La Niña (from 6.9 to 4.6) is found in such a case. In addition, about 7.6 extreme El Niño events are produced per 70 years. This is nearly twice as many as that in the standard run and is in accordance with the observations, where 3 out of the total four extreme El Niño events occurred from 1980 to 2000. Notably, such a result is consistent with the climate projection that an increased frequency of extreme El Niño events will appear due to the greenhouse warming since a projected surface warming over the EP is faster than that in the surrounding ocean waters (Cai et al., 2014). Next, if the decadal variability is set to be $I \equiv 1$, then the model mimics the situation when the Walker circulation and zonal thermocline slope are relatively strong, similar to the period after 2000. In such a scenario, more CP El Niño events (from 10 to 20.6) are found in the model simulation as a natural consequence of the strengthened zonal advection feedback. Similarly, less multi-year El Niño (from 10.5 to 9.6) and multi-year La Niña (from 6.9 to 5.2) are generated (Iwakiri & Watanabe, 2022). In addition, there remain only 1.3 extreme El Niño events per 70 years since the overall occurrence of the EP events becomes lower. These findings further indicate that the difference between the positive and negative phases of ENSO is weakened. As a result, the PDF of the EP SST becomes closer to Gaussian, which is fundamentally different from the observed non-Gaussian PDF with a fat tail.

The next analysis study is about the effect of the multiplicative noise $\sigma_p(T_C)$ in the stochastic wind burst process. The multiplicative noise is one of the main contributors to the asymmetry of the EP type of El Niño. If an additive noise (i.e., setting σ_p as a constant) is adopted, the PDF of the simulated EP SST becomes more symmetric and Gaussian. This is very different from the observations, where the amplitude of the extreme El Niño is typically larger than that of the strongest La Niña.

Finally, the nonlinear damping in the CP region is crucial to the ENSO dynamics and statistics. According to the observations, the asymmetry concerning the SST PDF in the CP is reversed compared with that in the EP. That is, the amplitude of the negative phase of the CP SST is generally stronger than that of the positive one, which leads to a negative skewness of the CP SST PDF. Such a negative skewness is accurately recovered with the help of the nonlinear function of α_q with the non-zero symmetric axis. On the other hand, the nonlinear damping in the CP region also plays a vital role in suppressing the amplitude of the strong CP events since the damping becomes more significant as the amplitude of the SST anomaly. As a result, the system favors the small and moderate SST anomalies, and a reduced kurtosis appears for the CP SST PDF.

5 Conclusions and Discussion

This paper develops a simple multiscale stochastic ICM to capture the ENSO diversity and complexity. The model highlights the interconnections between intraseasonal, interannual, and decadal variabilities. It also exploits suitable stochastic processes to facilitate the realistic simulation of the ENSO. The model succeeds in reproducing the spatiotemporal dynamical evolution of different types of ENSO events. It also accurately recovers the strongly non-Gaussian probability density function, the seasonal phase locking, the power spectrum, and the temporal autocorrelation function of the SST anomalies in all the three Niño regions (3, 3.4 and 4) across the equatorial Pacific. Furthermore, both the composites of the SST anomalies for various ENSO events and the strength-location bivariate distribution of equatorial Pacific SST maxima for the El Niño events from the model simulation highly resemble those from the observations. These desirable features of the model are essential for realistically simulating different ENSO events. They are also the prerequisites for the unbiased statistical forecast of the ENSO complexity.

Variable	Unit	Unit Value
x zonal axis	$[y]/\delta$	15000km
y atmospheric meridional axis	$\sqrt{c_A/\beta}$	1500km
Y oceanic meridional axis	$\sqrt{c_O/\beta}$	330km
t interannual time axis	$[t]$	34days
u zonal wind speed	δc_A	5ms^{-1}
v meridional wind speed	$\delta[u]$	0.5ms^{-1}
θ potential temperature	15δ	1.5K
E_q latent heating	$[\theta]/[t]$	0.45K.day^{-1}
U zonal current speed	$c_O\delta_O$	0.25ms^{-1}
V meridional current speed	$\delta\sqrt{c}[U]$	0.56cms^{-1}
H thermocline depth	$H_O\delta_O$	20.8m
T sea surface temperature	$[\theta]$	1.5K
a_p wind burst amplitude	$[u]$	5ms^{-1}

Table A1. Model variables, definitions and units.

It is worthwhile to point out that the stochastic ICM developed here shares many common features with the conceptual model in N. Chen et al. (2022). Both models include three time scales, where the decadal variability modulates the solution that alternates between the EP- and the CP-dominant regimes. At the same time, the intraseasonal wind bursts trigger most of the irregularities and extreme events. The underlying principles of incorporating stochastic wind bursts and the nonlinearity into both models also appear in a similar fashion. Nevertheless, the ICM emphasizes more sophisticated physics and includes many additional dynamical properties. It also involves spatially-extended structures, which allow a better understanding and potentially an improved forecast of the spatiotemporal patterns.

A few important topics remain as future work. First, the intraseasonal model adopted here is a one-dimensional simple stochastic process where the spatial structure is prescribed and fixed. A more realistic intraseasonal model can be a spatially-extended (stochastic) model for the wind bursts and the MJO; for example, one of the models in D. Yang and Ingersoll (2013); Wang et al. (2016); Adames and Kim (2016); Thual et al. (2018). A dynamical intraseasonal model allows the wind bursts and the MJO to have realistic spatial propagation mechanisms from the Indian Ocean to the WP. Such a coupled model will also help us understand the coupling between the MJO and the ENSO. Second, the model developed here has a symmetric meridional structure because only the leading meridional basis function is utilized in the meridionally truncated system. Yet, both the wind bursts and the ENSO have certain meridionally asymmetric features, which could be essential to account for the negative feedback associated with off-equatorial Rossby waves (Kirtman, 1997; Capotondi et al., 2006) or the effect of off-equatorial influences, for example, the north and south Pacific meridional modes (Chiang & Vimont, 2004; Zhang et al., 2014). Therefore, incorporating additional meridional basis functions into the model is a natural extension of the current system. Third, the ICM developed here applies to the forecast of different ENSO events. In particular, the ICM can be combined with the conceptual model in N. Chen et al. (2022) (and possibly the coupled MJO-ENSO model to be developed as well) for the multi-model data assimilation and forecast, which advances the understanding of the role of each model and each component in improving the forecast of the ENSO complexity.

Appendix A Variables and Parameters

The definitions and units of the model variables are listed in Table A1. The parameter values are summarized in Table A2.

Parameter	Value
ϵ Froude number	0.4
δ long-wave scaling	0.1
δ_O arbitrary constant	0.1
c_A atmospheric phase speed	$50\text{ms}^{-}1$
c_O oceanic phase speed	$2.5\text{ms}^{-}1$
c ratio of oceanic/atmospheric phase speed	0.05
c_1 modified ratio of phase speed	0.15
β beta-plane parameter	$2.28\ 10^{-11}\text{m}^{-1}\text{s}^{-1}$
g' reduced gravity	0.03ms^{-2}
H_O mean thermocline depth	50m
ρ_O ocean density	$1000\ \text{kg.m}^{-3}$
χ_A atmospheric meridional projection coefficient	0.31
χ_O oceanic meridional projection coefficient	1.38
L_A equatorial belt length	8/3
L_O equatorial Pacific length	1.2
$\bar{Q}$ mean vertical moisture gradient	0.9
$\bar{T}$ mean SST	16.6 (which is 25^oC)
α_q latent heating factor	$\alpha_q = q_c q_e \exp(q_e \bar{T})/\tau_q \times \beta_1(T) \times \beta_2(t)$
$\beta(T)$ state dependent component in α_q	$\beta_1(T) = 1.8 - \eta_2/3 + (0.2 + \lvert T_C + 0.4\rvert \times \eta_2)^2/5$
$\beta(T)$ seasonal dependent component in α_q	$\beta_2(T) = 1 + 0.5\sin(2\pi(t - 1/12)) + 0.1\sin(2\pi t)\eta_2$ $-0.0625\sin(4\pi(t - 3/12))\eta_1$
q_c latent heating multiplier coefficient	7
q_e latent heating exponential coefficient	0.093
τ_q latent heating adjustment rate	15
γ wind stress coefficient	6.53
r_W western boundary reflection coefficient	0.5
r_E eastern boundary reflection coefficient	1
ζ latent heating exchange coefficient	8.7
c_2 mean correction coefficient	0.1
η profile of thermocline feedback	$\eta(x) = 1.3 + (1.1 \times \tanh(7.5(x - L_O/3)))$
η_2 profile of zonal advective feedback	$\eta_2(x) = \max(0, 4\exp(-(x - L_O/(7/3))^2/0.1) \times 0.9)$
d_p wind burst damping	1.12 (which is 1mon^{-1})
s_p wind burst zonal structure	$s_p(x) = \exp(-45(x - L_O/4)^2)$
$\sigma_p(T_C)$ wind burst noise coefficient	$\sigma_p(T_C) = 1.6(\tanh(T_C) + 1)(1 + 0.6\cos(2\pi t))(1 - 0.75I)$
λ damping of decadal variability	0.0186 (which is 5year^{-1})
m mean of I	0.5

Table A2. Model parameter values.

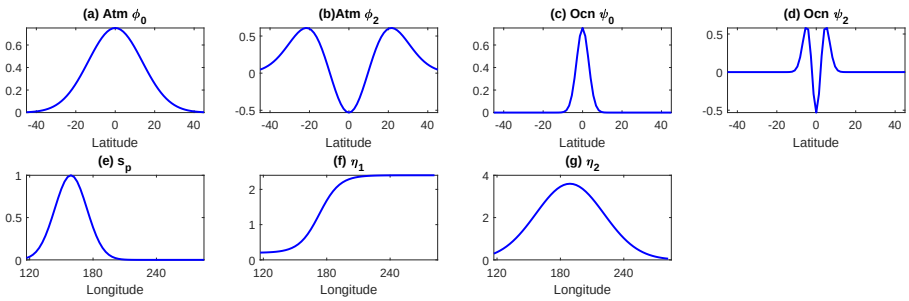

Figure A1. Panels (a)–(d): Spatial structure functions of the meridional bases $\phi_0(y)$, $\phi_2(y)$, $\psi_0(y)$ and $\psi_2(y)$. Panels (e)–(g): Spatial structure functions of $s_p(x)$, $\eta_1(x)$ and $\eta_2(x)$.

As was stated in Section 2.1, different parabolic cylinder functions in the ocean and atmosphere were used in the coupled model. Their profiles are shown in Figure A1. The atmospheric parabolic cylinder functions read $\phi_0(y) = (\pi)^{-1/4}\exp(-y^2/2)$, $\phi_2(y) = (4\pi)^{-1/4}(2y^2-1)\exp(-y^2/2)$. The ocean parabolic cylinder functions read $\psi_m(Y)$, which have the same profiles as the atmospheric ones but depend on the oceanic meridional axis Y.

To couple the ocean and atmosphere, projection coefficients are introduced, which read $\chi_A = \int_{-\infty}^{+\infty}\phi_0(y)\phi_0(y/\sqrt{c})\,\mathrm{d}y$ and $\chi_O = \int_{-\infty}^{+\infty}\psi_0(Y)\psi_0(Y/\sqrt{c}Y)\,\mathrm{d}Y$. The atmosphere uses a truncation of the Kelvin and first Rossby atmospheric equatorial waves of amplitude K_A and R_A. The ocean uses a truncation of zonal wind stress forcing to ψ_0, $\tau_x = \tau_x\psi_0$. This is known to excite only the Kelvin and first Rossby oceanic waves of amplitude K_O and R_O. Similarly, for the SST model, a truncation ψ_0, $T = T\psi_0$ is utilized. Then, the deterministic and linear part of the ENSO model truncated meridionally yields (4)–(6).

Appendix B Parameters for the Two Different Linear Solutions

The model starts with a deterministic and linear coupled interannual atmosphere, ocean, and SST system. Before the two stochastic processes on the other two time scales are further incorporated, confirming that the linear model can generate the basic solutions of the two types of ENSO events under different parameter settings is crucial. In addition, the potential difference should be as slight as possible for the physical interpretation.

In this model, the behavior of the leading mode is mainly determined by the relative amplitude between the zonal advective feedback and the thermocline feedback, which is consistent with the observational analyses. For this purpose, the only change of the setting is the strength of the zonal advective feedback, i.e., η_2. Specifically, for the linear solution corresponding to the CP ENSO regime, $\eta_2(x) = \max(0, 4\exp(-(x-L_O/(7/3))^2/0.05)\times 0.9)$ is utilized (Panel (b) of Figure 2), while for that corresponding to the EP ENSO regime, $\eta_2(x) = \max(0, 4\exp(-(x-L_O/(7/3))^2/0.05)\times 0.9)\times 0.3$ is adopted (Panel (a) of Figure 2), which is 30% of the one in the CP ENSO regime. Figure B1 illustrates the spectrum of the eigenmodes as a function of the frequency and the growth rate. The two panels show the EP and CP El Niño dominant cases, corresponding to the two panels in Figure 2.

Appendix C Stochastic Process with Multiplicative Noise for the Decadal Variability

The decadal variability influences the occurrence frequency of the two types of El Niño and, thus, the ENSO complexity. A stochastic model is introduced for the decadal variability, which depicts the strength of the background Walker circulation and affects the related zonal

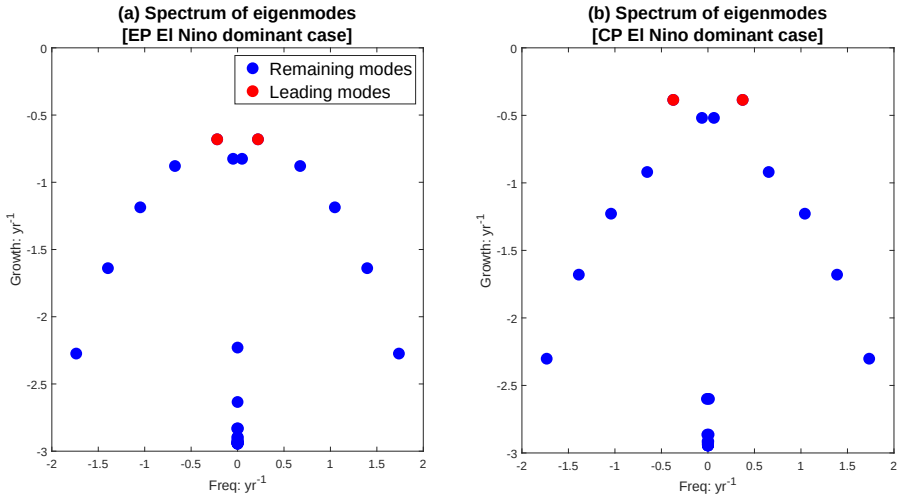

Figure B1. The spectrum of the eigenmodes as a function of the frequency (x-axis; unit: year^{-1}) and the growth rate (y-axis; unit: year^{-1}). Panels (a)–(b) here show the EP and CP El Niño dominant cases, corresponding to the two panels in Figure 2.

advective feedback. In the decadal model (9), a state-dependent (i.e., multiplicative) noise coefficient $\sigma_I(I)$ is adopted that allows I to be non-negative, which comes from the fact that the trade wind in the lower level of the Walker circulation in the decadal time scale is easterly. Here, as only limited data for the decadal variability is available, a uniform distribution function of I is adopted in the model. This is based on the fact that the uniform distribution is the maximum entropy solution for a function in the finite interval without additional information (Kapur & Kesavan, 1992; Branicki et al., 2013; Majda & Wang, 2006). The parameter m is the mean of I, which can be inferred directly from the data. The damping parameter λ can be determined by taking the inverse of the decorrelation time, which is defined as

$$\tau = \lim_{T\to\infty} \int_0^T ACF(t)\,\mathrm{d}t \qquad \text{with} \qquad ACF(t) = \lim_{T\to\infty} \frac{1}{T} \int_0^T \frac{I(t+t')I(t')}{var(I)}\,\mathrm{d}t',$$

where T here is the time not SST. A sufficiently large T is used as a numerical approximation. Finally, the multiplicative noise coefficient $\sigma_I(I)$ is determined in the following way (Averina & Artemiev, 1988)

$$\sigma_I^2(I) = \frac{-2\lambda}{p(I)} \int_{-\infty}^{I} \left(s - \frac{m}{\lambda}\right) p(s)\,\mathrm{d}s.$$

Data availability statement

The monthly ocean temperature and current data were downloaded from the National Centers for Environmental Prediction Global Ocean Data Assimilation System at https://www.esrl.noaa.gov/psd/data/gridded/data.godas.html (Behringer & Xue, 2004). The programs and data for the model can be obtained from this site https://doi.org/10.5281/zenodo.6797996 (N. Chen & Fang, 2022).

Acknowledgments

The research of N.C. is partially funded by the Office of VCRGE at UW-Madison and ONR N00014-21-1-2904. The research of X.F. is supported by Guangdong Major Project of

Basic and Applied Basic Research (Grant No. 2020B0301030004), the Ministry of Science and Technology of the People's Republic of China (Grant No. 2020YFA0608802) and the National Natural Science Foundation of China (Grant Nos. 42192564 and 41805045).

References

Adames, Á. F., & Kim, D. (2016). The MJO as a dispersive, convectively coupled moisture wave: Theory and observations. *Journal of the Atmospheric Sciences*, *73*(3), 913–941.

Anderson, B. T., Perez, R. C., & Karspeck, A. (2013). Triggering of el niño onset through trade wind–induced charging of the equatorial pacific. *Geophysical Research Letters*, *40*(6), 1212–1216.

Ashok, K., Behera, S. K., Rao, S. A., Weng, H., & Yamagata, T. (2007). El Niño Modoki and its possible teleconnection. *Journal of Geophysical Research: Oceans*, *112*(C11).

Averina, T., & Artemiev, S. (1988). Numerical solution of systems of stochastic differential equations. *Russian Journal of Numerical Analysis and Mathematical Modelling*, *3*(4), 267–286.

Barnston, A. G., Tippett, M. K., L'Heureux, M. L., Li, S., & DeWitt, D. G. (2012). Skill of real-time seasonal ENSO model predictions during 2002–11: Is our capability increasing? *Bulletin of the American Meteorological Society*, *93*(5), 631–651.

Behringer, D., & Xue, Y. (2004). Evaluation of the global ocean data assimilation system at NCEP: The Pacific Ocean [dataset]. In *Proc. eighth symp. on integrated observing and assimilation systems for atmosphere, oceans, and land surface.*

Biello, J. A., & Majda, A. J. (2006). Modulating synoptic scale convective activity and boundary layer dissipation in the IPESD models of the Madden–Julian oscillation. *Dynamics of atmospheres and oceans*, *42*(1-4), 152–215.

Bjerknes, J. (1969). Atmospheric teleconnections from the equatorial pacific. *Monthly Weather Review*, *97*(3), 163–172.

Branicki, M., Chen, N., & Majda, A. J. (2013). Non-Gaussian test models for prediction and state estimation with model errors. *Chinese Annals of Mathematics, Series B*, *34*(1), 29–64.

Cai, W., Borlace, S., Lengaigne, M., Van Rensch, P., Collins, M., Vecchi, G., ... others (2014). Increasing frequency of extreme El Niño events due to greenhouse warming. *Nature Climate Change*, *4*(2), 111–116.

Cane, M. A., Sarachik, E., Moore, D., & Sarachik, E. (1981). The response of a linear baroclinic equatorial ocean to periodic forcing. *Journal of Marine Research*, *39*(4), 651–693.

Capotondi, A., & Ricciardulli, L. (2021). The influence of pacific winds on enso diversity. *Scientific reports*, *11*(1), 1–11.

Capotondi, A., & Sardeshmukh, P. D. (2015). Optimal precursors of different types of ENSO events. *Geophysical Research Letters*, *42*(22), 9952–9960.

Capotondi, A., Sardeshmukh, P. D., & Ricciardulli, L. (2018). The nature of the stochastic wind forcing of ENSO. *Journal of Climate*, *31*(19), 8081–8099.

Capotondi, A., Wittenberg, A., & Masina, S. (2006). Spatial and temporal structure of tropical Pacific interannual variability in 20th century coupled simulations. *Ocean Modelling*, *15*(3-4), 274–298.

Capotondi, A., Wittenberg, A. T., Kug, J.-S., Takahashi, K., & McPhaden, M. J. (2020). Enso diversity. *El Niño Southern Oscillation in a changing climate*, 65–86.

Capotondi, A., Wittenberg, A. T., Newman, M., Di Lorenzo, E., Yu, J.-Y., Braconnot, P., ... others (2015). Understanding ENSO diversity. *Bulletin of the American Meteorological Society*, *96*(6), 921–938.

Chen, D., & Cane, M. A. (2008). El Niño prediction and predictability. *Journal of Computational Physics*, *227*(7), 3625–3640.

Chen, D., Lian, T., Fu, C., Cane, M. A., Tang, Y., Murtugudde, R., ... Zhou, L. (2015). Strong influence of westerly wind bursts on El Niño diversity. *Nature Geoscience*, *8*(5), 339–345.

Chen, N., & Fang, X. (2022). Model programs for "a simple multiscale intermediate coupled stochastic model for El Niño diversity and complexity" [software]. *Zenodo*. doi: 10 .5281/zenodo.6797996

Chen, N., Fang, X., & Yu, J.-Y. (2022). A multiscale model for el niño complexity. *npj Climate and Atmospheric Science*, *5*(1), 1–13.

Chen, N., & Majda, A. J. (2016). Simple dynamical models capturing the key features of the central pacific el niño. *Proceedings of the National Academy of Sciences*, *113*(42), 11732–11737.

Chen, N., Majda, A. J., & Thual, S. (2018). Observations and mechanisms of a simple stochastic dynamical model capturing el niño diversity. *Journal of Climate*, *31*(1), 449–471.

Chiang, J. C., & Vimont, D. J. (2004). Analogous Pacific and Atlantic meridional modes of tropical atmosphere–ocean variability. *Journal of Climate*, *17*(21), 4143–4158.

Dieppois, B., Capotondi, A., Pohl, B., Chun, K. P., Monerie, P.-A., & Eden, J. (2021). ENSO diversity shows robust decadal variations that must be captured for accurate future projections. *Communications Earth & Environment*, *2*(1), 1–13.

Fang, X., & Chen, N. (2022). Quantifying the predictability of enso complexity using a statistically accurate multiscale stochastic model and information theory. *arXiv preprint arXiv:2203.02657*.

Fang, X., & Mu, M. (2018). A three-region conceptual model for central Pacific El Niño including zonal advective feedback. *Journal of Climate*, *31*(13), 4965–4979.

Fang, X., & Zheng, F. (2018). Simulating eastern-and central-pacific type ENSO using a simple coupled model. *Advances in Atmospheric Sciences*, *35*(6), 671–681.

Fang, X., Zheng, F., & Zhu, J. (2015). The cloud-radiative effect when simulating strength asymmetry in two types of El Niño events using CMIP5 models. *Journal of Geophysical Research: Oceans*, *120*(6), 4357–4369.

Fedorov, A. V., & Philander, S. G. (2001). A stability analysis of tropical ocean–atmosphere interactions: Bridging measurements and theory for El Niño. *Journal of Climate*, *14*(14), 3086–3101.

Freund, M. B., Henley, B. J., Karoly, D. J., McGregor, H. V., Abram, N. J., & Dommenget, D. (2019). Higher frequency of central Pacific El Niño events in recent decades relative to past centuries. *Nature Geoscience*, *12*(6), 450–455.

Gardiner, C. (2009). *Stochastic methods* (Vol. 4). Springer Berlin.

Gebbie, G., Eisenman, I., Wittenberg, A., & Tziperman, E. (2007). Modulation of westerly wind bursts by sea surface temperature: A semistochastic feedback for enso. *Journal of the Atmospheric Sciences*, *64*(9), 3281–3295.

Gebbie, G., & Tziperman, E. (2009). Predictability of sst-modulated westerly wind bursts. *Journal of climate*, *22*(14), 3894–3909.

Geng, L., & Jin, F.-F. (2022). Enso diversity simulated in a revised cane-zebiak model. *Frontiers in Earth Science*, *10*, 899323.

Gill, A. E. (1980). Some simple solutions for heat-induced tropical circulation. *Quarterly Journal of the Royal Meteorological Society*, *106*(449), 447–462.

Ham, Y.-G., & Kug, J.-S. (2012). How well do current climate models simulate two types of El Niño? *Climate Dynamics*, *39*(1-2), 383–398.

Harrison, D., & Vecchi, G. A. (1997). Westerly wind events in the tropical pacific, 1986–95. *Journal of Climate*, *10*(12), 3131–3156.

Hayashi, M., Jin, F.-F., & Stuecker, M. F. (2020). Dynamics for El Niño-La Niña asymmetry constrain equatorial-Pacific warming pattern. *Nature communications*, *11*(1), 1–10.

Hendon, H. H., Wheeler, M. C., & Zhang, C. (2007). Seasonal dependence of the MJO–ENSO relationship. *Journal of Climate*, *20*(3), 531–543.

Hu, S., & Fedorov, A. V. (2016). Exceptionally strong easterly wind burst stalling El Niño of 2014. *Proceedings of the National Academy of Sciences*, *113*(8), 2005–2010.

Hu, Z.-Z., Kumar, A., Jha, B., Wang, W., Huang, B., & Huang, B. (2012). An analysis of warm pool and cold tongue El Niños: Air–sea coupling processes, global influences, and recent trends. *Climate Dynamics*, *38*(9), 2017–2035.

Iwakiri, T., & Watanabe, M. (2022). Multi-year ENSO dynamics as revealed in observations, climate model simulations, and the linear recharge oscillator. *Journal of Climate*, 1–42.

Jin, E. K., Kinter, J. L., Wang, B., Park, C.-K., Kang, I.-S., Kirtman, B., ... others (2008). Current status of ENSO prediction skill in coupled ocean–atmosphere models. *Climate Dynamics*, *31*(6), 647–664.

Jin, F.-F. (1997a). An equatorial ocean recharge paradigm for ENSO. Part I: Conceptual model. *Journal of the Atmospheric Sciences*, *54*(7), 811–829.

Jin, F.-F. (1997b). An equatorial ocean recharge paradigm for enso. part ii: A stripped-down coupled model. *Journal of the Atmospheric Sciences*, *54*(7), 830–847.

Jin, F.-F., An, S.-I., Timmermann, A., & Zhao, J. (2003). Strong El Niño events and nonlinear dynamical heating. *Geophysical Research Letters*, *30*(3), 20–1.

Johnson, N. C. (2013). How many enso flavors can we distinguish? *Journal of Climate*, *26*(13), 4816–4827.

Kang, S. M., Xie, S.-P., Shin, Y., Kim, H., Hwang, Y.-T., Stuecker, M. F., ... Hawcroft, M. (2020). Walker circulation response to extratropical radiative forcing. *Science Advances*, *6*(47), eabd3021.

Kao, H.-Y., & Yu, J.-Y. (2009). Contrasting eastern-Pacific and central-Pacific types of ENSO. *Journal of Climate*, *22*(3), 615–632.

Kapur, J. N., & Kesavan, H. K. (1992). Entropy optimization principles and their applications. In *Entropy and energy dissipation in water resources* (pp. 3–20). Springer.

Kim, J.-S., Kim, K.-Y., & Yeh, S.-W. (2012). Statistical evidence for the natural variation of the central pacific el niño. *Journal of Geophysical Research: Oceans*, *117*(C6).

Kirtman, B. P. (1997). Oceanic rossby wave dynamics and the ENSO period in a coupled model. *Journal of climate*, *10*(7), 1690–1704.

Kug, J.-S., Choi, J., An, S.-I., Jin, F.-F., & Wittenberg, A. T. (2010). Warm pool and cold tongue El Niño events as simulated by the GFDL 2.1 coupled GCM. *Journal of Climate*, *23*(5), 1226–1239.

Kug, J.-S., Ham, Y.-G., Lee, J.-Y., & Jin, F.-F. (2012). Improved simulation of two types of El Niño in CMIP5 models. *Environmental Research Letters*, *7*(3), 034002.

Kug, J.-S., Jin, F.-F., & An, S.-I. (2009). Two types of El Niño events: cold tongue El Niño and warm pool El Niño. *Journal of Climate*, *22*(6), 1499–1515.

Larkin, N. K., & Harrison, D. (2005). Global seasonal temperature and precipitation anomalies during El Niño autumn and winter. *Geophysical Research Letters*, *32*(16).

Latif, M., Anderson, D., Barnett, T., Cane, M., Kleeman, R., Leetmaa, A., ... Schneider, E. (1998). A review of the predictability and prediction of enso. *Journal of Geophysical Research: Oceans*, *103*(C7), 14375–14393.

Levine, A., Jin, F.-F., & McPhaden, M. J. (2016). Extreme noise–extreme El Niño: How state-dependent noise forcing creates El Niño–La Niña asymmetry. *Journal of Climate*, *29*(15), 5483–5499.

Lian, T., Chen, D., Tang, Y., & Jin, B. (2014). A theoretical investigation of the tropical Indo-Pacific tripole mode. *Science China Earth Sciences*, *57*(1), 174–188.

Lin, J.-L. (2007). The double-itcz problem in ipcc ar4 coupled gcms: Ocean–atmosphere feedback analysis. *Journal of Climate*, *20*(18), 4497–4525.

Majda, A. J. (2003). *Introduction to pdes and waves for the atmosphere and ocean* (Vol. 9). American Mathematical Soc.

Majda, A. J., & Chen, N. (2018). Model error, information barriers, state estimation and prediction in complex multiscale systems. *Entropy*, *20*(9), 644.

Majda, A. J., & Stechmann, S. N. (2009). The skeleton of tropical intraseasonal oscillations. *Proceedings of the National Academy of Sciences*, *106*(21), 8417–8422.

Majda, A. J., & Wang, X. (2006). *Nonlinear dynamics and statistical theories for basic geophysical flows*. Cambridge University Press.

Matsuno, T. (1966). Quasi-geostrophic motions in the equatorial area. *Journal of the Meteorological Society of Japan. Ser. II*, *44*(1), 25–43.

McPhaden, M. J., Lee, T., & McClurg, D. (2011). El Niño and its relationship to changing background conditions in the tropical Pacific ocean. *Geophysical Research Letters*, *38*(15).

McPhaden, M. J., Zebiak, S. E., & Glantz, M. H. (2006). ENSO as an integrating concept in earth science. *Science*, *314*(5806), 1740–1745.

Mitchell, T. P., & Wallace, J. M. (1992). The annual cycle in equatorial convection and sea surface temperature. *Journal of Climate*, *5*(10), 1140–1156.

Neelin, J. D., Battisti, D. S., Hirst, A. C., Jin, F.-F., Wakata, Y., Yamagata, T., & Zebiak, S. E. (1998). ENSO theory. *Journal of Geophysical Research: Oceans*, *103*(C7), 14261–14290.

Planton, Y. Y., Guilyardi, E., Wittenberg, A. T., Lee, J., Gleckler, P. J., Bayr, T., ... others (2021). Evaluating climate models with the clivar 2020 ENSO metrics package. *Bulletin of the American Meteorological Society*, *102*(2), E193–E217.

Power, S., Lengaigne, M., Capotondi, A., Khodri, M., Vialard, J., Jebri, B., ... others (2021). Decadal climate variability in the tropical Pacific: Characteristics, causes, predictability, and prospects. *Science*, *374*(6563), eaay9165.

Puy, M., Vialard, J., Lengaigne, M., & Guilyardi, E. (2016). Modulation of equatorial pacific westerly/easterly wind events by the madden–julian oscillation and convectively-coupled rossby waves. *Climate Dynamics*, *46*(7), 2155–2178.

Ropelewski, C. F., & Halpert, M. S. (1987). Global and regional scale precipitation patterns associated with the El Niño/Southern Oscillation. *Monthly Weather Review*, *115*(8), 1606–1626.

Santoso, A., Hendon, H., Watkins, A., Power, S., Dommenget, D., England, M. H., ... others (2019). Dynamics and predictability of El Niño–Southern Oscillation: an Australian perspective on progress and challenges. *Bulletin of the American Meteorological Society*, *100*(3), 403–420.

Schopf, P. S., & Suarez, M. J. (1988). Vacillations in a coupled ocean–atmosphere model. *Journal of Atmospheric Sciences*, *45*(3), 549–566.

Seiki, A., & Takayabu, Y. N. (2007). Westerly wind bursts and their relationship with intraseasonal variations and ENSO. Part I: Statistics. *Monthly Weather Review*, *135*(10), 3325–3345.

Sohn, S.-J., Tam, C.-Y., & Jeong, H.-I. (2016). How do the strength and type of ENSO affect SST predictability in coupled models. *Scientific Reports*, *6*(1), 1–8.

Stechmann, S. N., & Majda, A. J. (2015). Identifying the skeleton of the Madden–Julian oscillation in observational data. *Monthly Weather Review*, *143*(1), 395–416.

Stein, K., Timmermann, A., Schneider, N., Jin, F.-F., & Stuecker, M. F. (2014). ENSO seasonal synchronization theory. *Journal of Climate*, *27*(14), 5285–5310.

Sullivan, A., Luo, J.-J., Hirst, A. C., Bi, D., Cai, W., & He, J. (2016). Robust contribution of decadal anomalies to the frequency of central-pacific El Niño. *Scientific reports*, *6*(1), 1–7.

Thual, S., Majda, A. J., & Chen, N. (2017). Seasonal synchronization of a simple stochastic dynamical model capturing El Niño diversity. *Journal of Climate*, *30*(24), 10047–10066.

Thual, S., Majda, A. J., & Chen, N. (2018). A tropical stochastic skeleton model for the MJO, El Niño, and dynamic Walker circulation: A simplified GCM. *Journal of Climate*, *31*(22), 9261–9282.

Thual, S., Majda, A. J., & Chen, N. (2019). Statistical occurrence and mechanisms of the 2014–2016 delayed super El Niño captured by a simple dynamical model. *Climate Dynamics*, *52*(3-4), 2351–2366.

Thual, S., Majda, A. J., Chen, N., & Stechmann, S. N. (2016). Simple stochastic model for El Niño with westerly wind bursts. *Proceedings of the National Academy of Sciences*, *113*(37), 10245–10250.

Timmermann, A., An, S.-I., Kug, J.-S., Jin, F.-F., Cai, W., Capotondi, A., ... others (2018). El Niño-Southern Oscillation complexity. *Nature*, *559*(7715), 535–545.

Tziperman, E., & Yu, L. (2007). Quantifying the dependence of westerly wind bursts on the large-scale tropical Pacific SST. *Journal of Climate*, *20*(12), 2760–2768.

Tziperman, E., Zebiak, S. E., & Cane, M. A. (1997). Mechanisms of seasonal–ENSO interaction. *Journal of the Atmospheric Sciences*, *54*(1), 61–71.

Vallis, G. K. (2016). Geophysical fluid dynamics: whence, whither and why? *Proceedings of the Royal Society A: Mathematical, Physical and Engineering Sciences*, *472*(2192), 20160140.

Vecchi, G. A., & Harrison, D. (2000). Tropical pacific sea surface temperature anomalies, el niño, and equatorial westerly wind events. *Journal of Climate*, *13*(11), 1814–1830.

Wang, B., Liu, F., & Chen, G. (2016). A trio-interaction theory for Madden–Julian oscillation. *Geoscience Letters*, *3*(1), 1–16.

Wang, B., Luo, X., Yang, Y.-M., Sun, W., Cane, M. A., Cai, W., ... Liu, J. (2019). Historical change of El Niño properties sheds light on future changes of extreme El Niño. *Proceedings of the National Academy of Sciences*, *116*(45), 22512–22517.

Wiedermann, M., Radebach, A., Donges, J. F., Kurths, J., & Donner, R. V. (2016). A climate network-based index to discriminate different types of el niño and la niña. *Geophysical Research Letters*, *43*(13), 7176–7185.

Wittenberg, A. T. (2009). Are historical records sufficient to constrain enso simulations? *Geophysical Research Letters*, *36*(12).

Xiang, B., Wang, B., & Li, T. (2013). A new paradigm for the predominance of standing central Pacific warming after the late 1990s. *Climate Dynamics*, *41*(2), 327–340.

Xie, R., & Fang, X. (2020). The unusual 2014–2016 El Niño events: Dynamics, prediction and enlightenments. *Science China Earth Sciences*, *63*(5), 626–633.

Xie, R., & Jin, F.-F. (2018). Two leading enso modes and el niño types in the zebiak–cane model. *Journal of Climate*, *31*(5), 1943–1962.

Yang, D., & Ingersoll, A. P. (2013). Triggered convection, gravity waves, and the MJO: A shallow-water model. *Journal of the atmospheric sciences*, *70*(8), 2476–2486.

Yang, Q., Majda, A. J., & Chen, N. (2021). ENSO diversity in a tropical stochastic skeleton model for the MJO, El Niño, and dynamic Walker circulation. *Journal of Climate*, 1–56.

Yu, J.-Y., & Kao, H.-Y. (2007). Decadal changes of ENSO persistence barrier in SST and ocean heat content indices: 1958–2001. *Journal of Geophysical Research: Atmospheres*, *112*(D13).

Yu, J.-Y., & Kim, S. T. (2013). Identifying the types of major El Niño events since 1870. *International Journal of Climatology*, *33*(8), 2105–2112.

Zebiak, S. E., & Cane, M. A. (1987). A model El Niño–Southern Oscillation. *Monthly Weather Review*, *115*(10), 2262–2278.

Zhang, H., Clement, A., & Di Nezio, P. (2014). The South Pacific meridional mode: A mechanism for ENSO-like variability. *Journal of Climate*, *27*(2), 769–783.

Zhao, S., Jin, F.-F., Long, X., & Cane, M. A. (2021). On the breakdown of enso's relationship with thermocline depth in the central-equatorial pacific. *Geophysical Research Letters*, *48*(9), e2020GL092335.

Zheng, F., Fang, X., Yu, J.-Y., & Zhu, J. (2014). Asymmetry of the Bjerknes positive feedback between the two types of El Niño. *Geophysical Research Letters*, *41*(21), 7651–7657.

Figure 1.

(a) Schematic Illustration of the Model Development

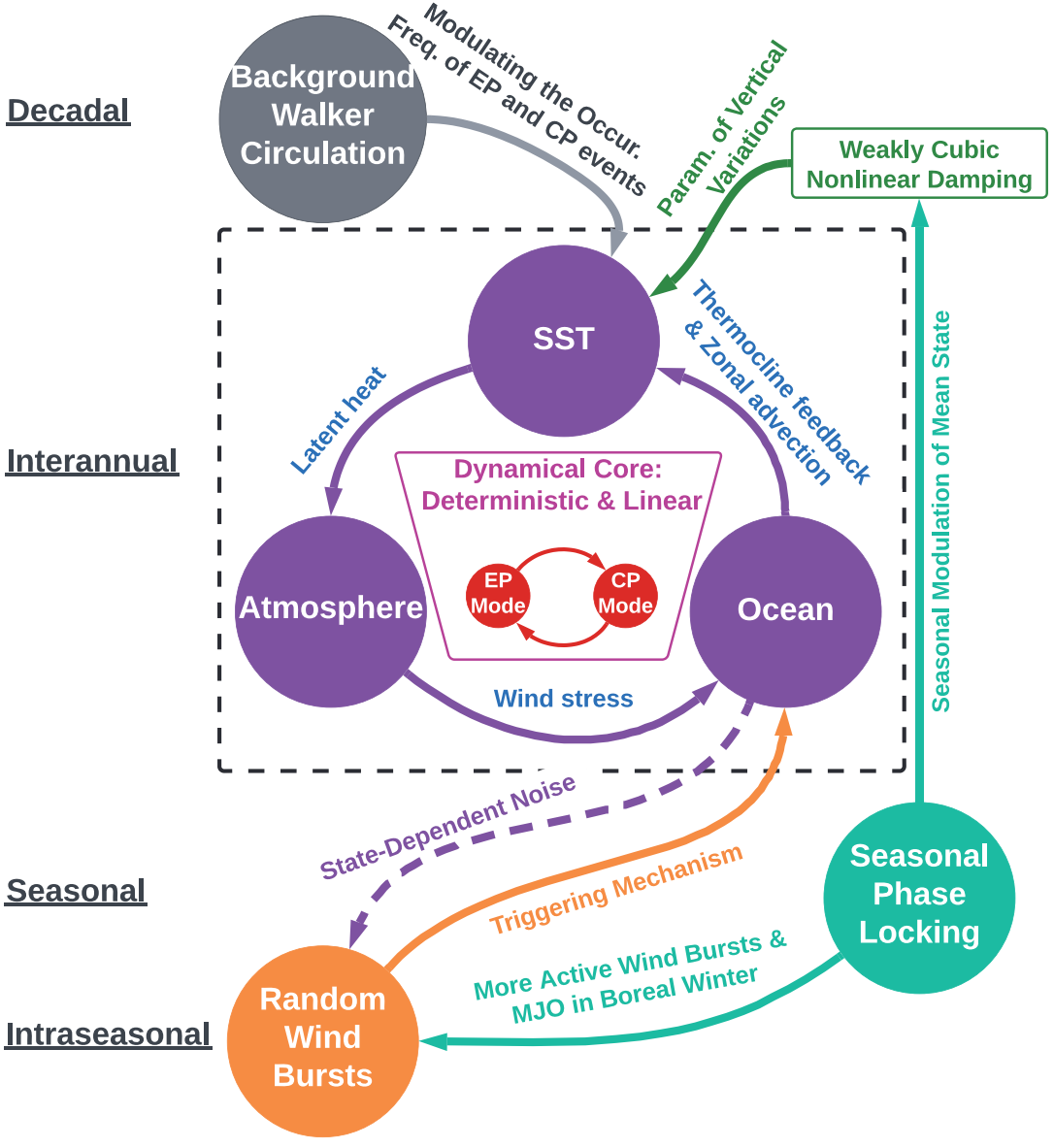

(b) Observed SST

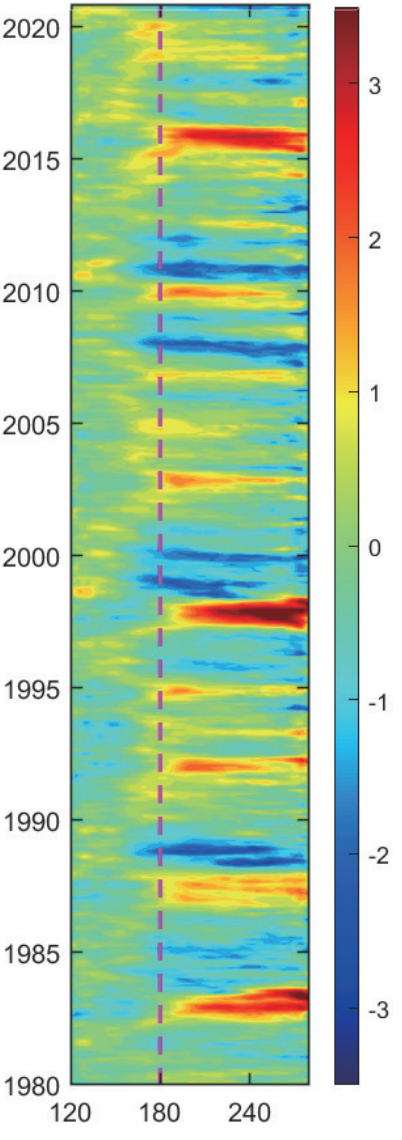

Figure 2.

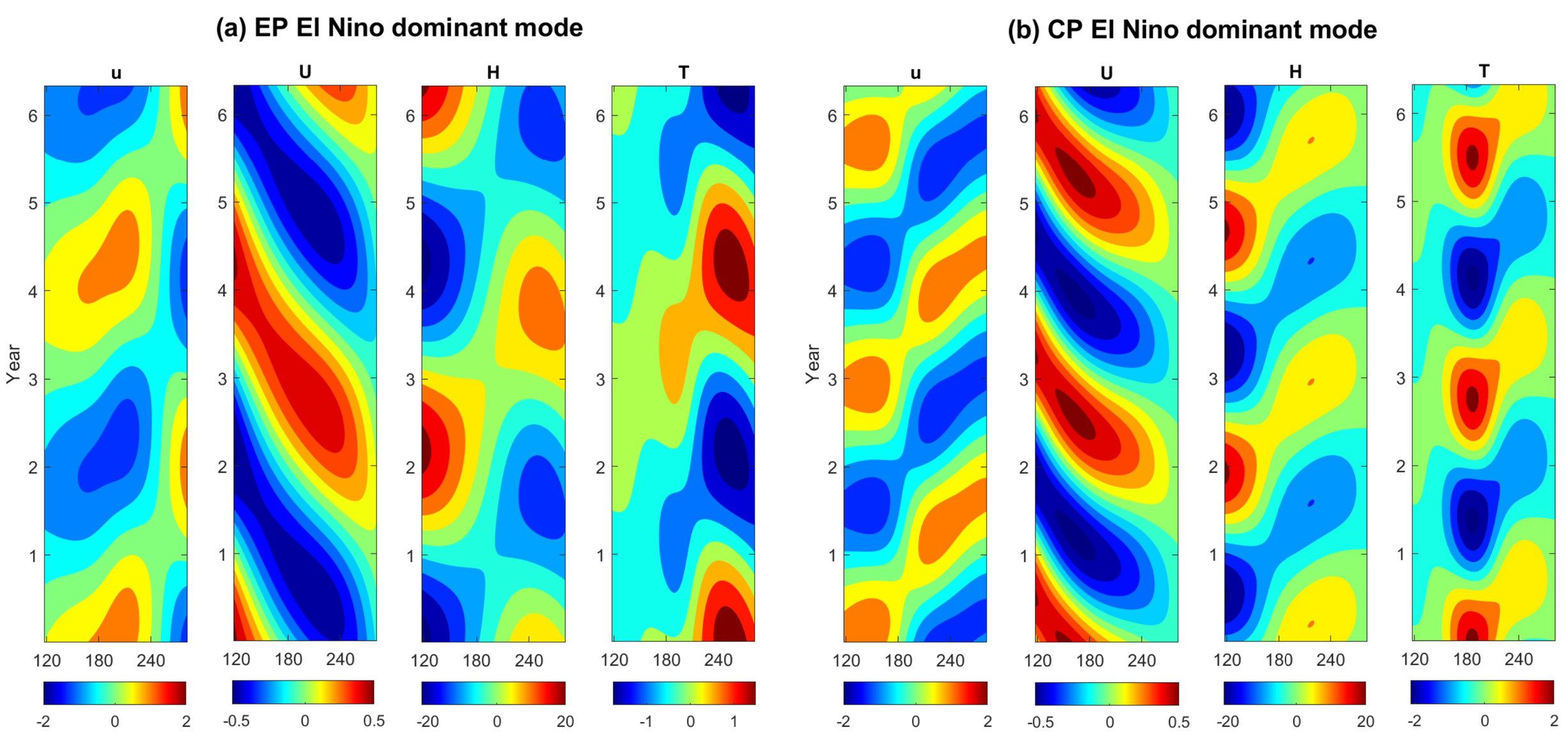
(a) EP El Nino dominant mode
(b) CP El Nino dominant mode
u
U
H
T
Year
1
2
3
4
5
6
120
180
240
-2
0
2
-0.5
0.5
-20
20
-1
1

Figure 3.

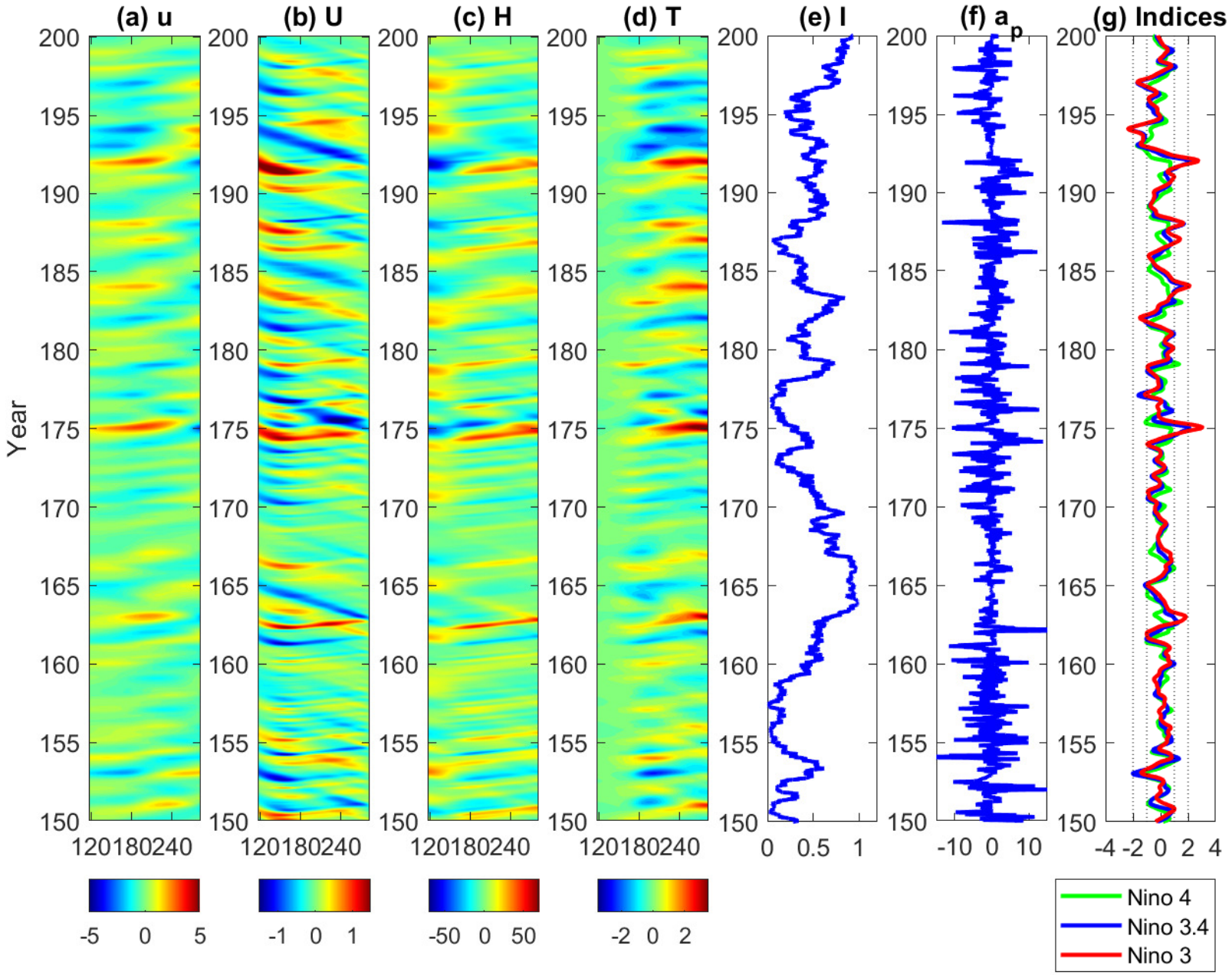
(a) u
(b) U
(c) H
(d) T
(e) I
(f) a p
(g) Indices
Year
200
195
190
185
180
175
170
165
160
155
150
120180240
-5 0 5
-1 0 1
-50 0 50
-2 0 2
0 0.5 1
-10 0 10
-4 -2 0 2 4
Nino 4
Nino 3.4
Nino 3

Figure 4.

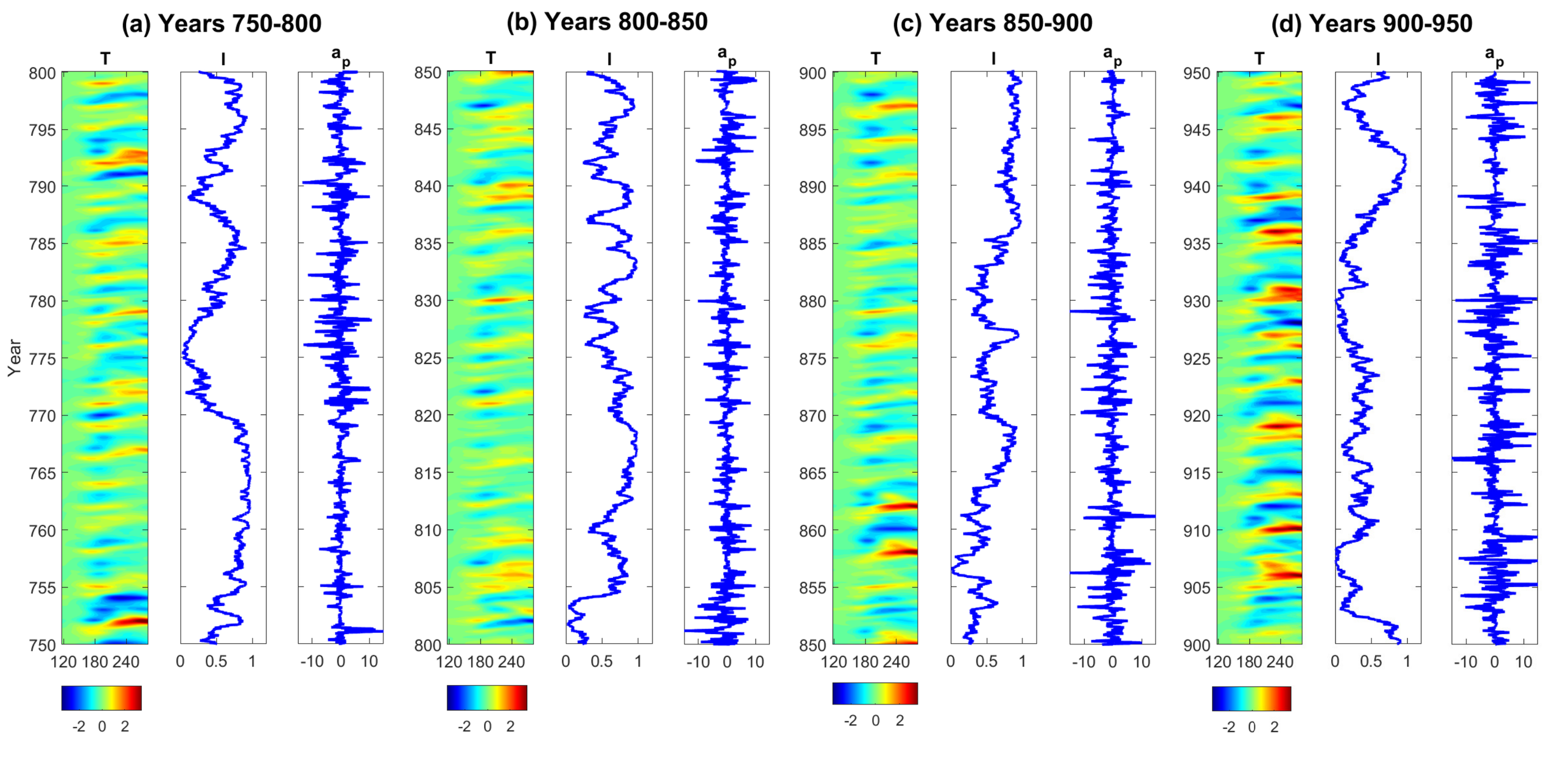
(a) Years 750-800
(b) Years 800-850
(c) Years 850-900
(d) Years 900-950
T
I
a_p
Year
800
795
790
785
780
775
770
765
760
755
750
850
845
840
835
830
825
820
815
810
805
800
900
895
890
885
880
875
870
865
860
855
850
950
945
940
935
930
925
920
915
910
905
900
120 180 240
0 0.5 1
-10 0 10
-2 0 2

Figure 5.

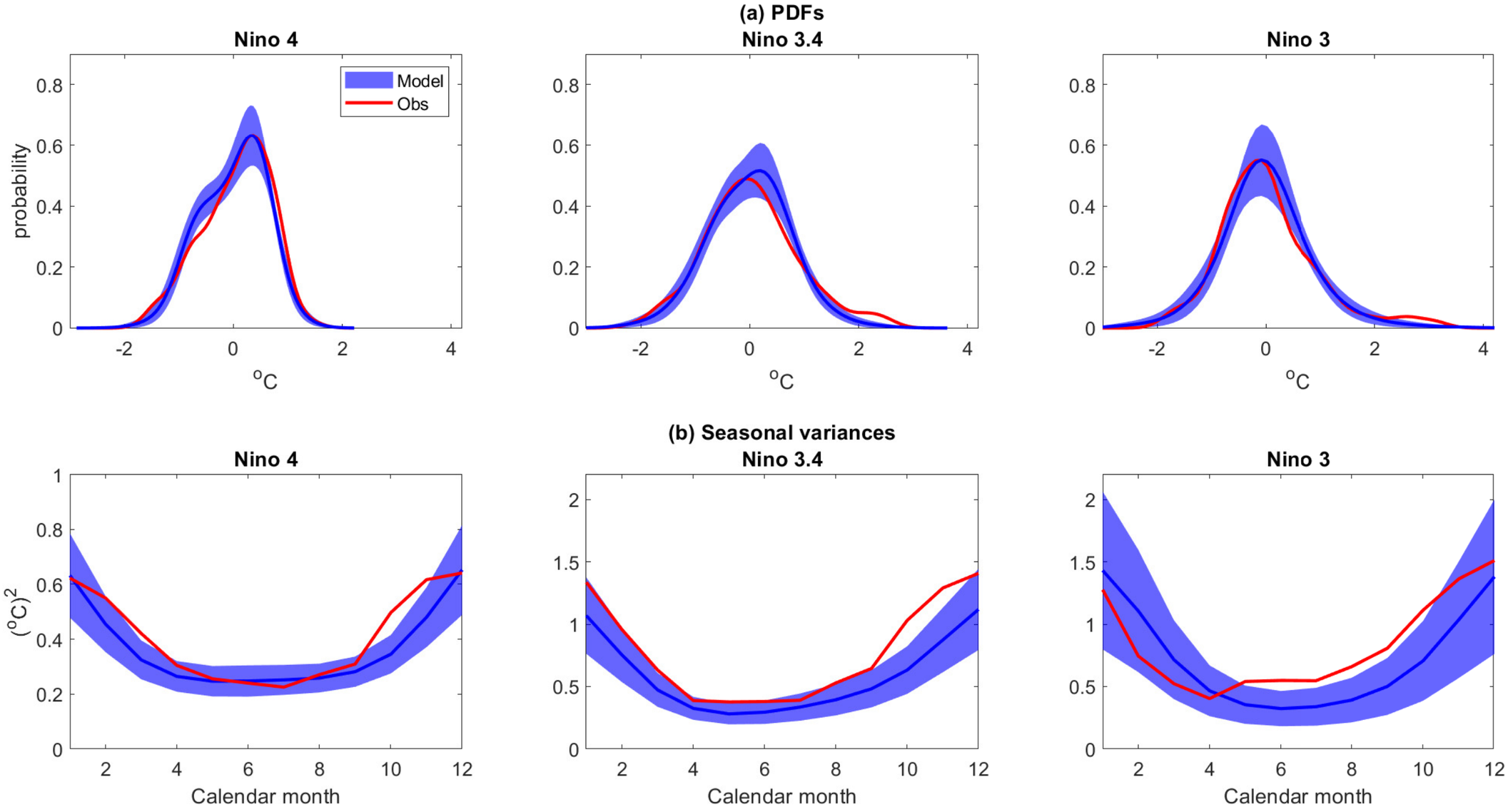
(a) PDFs
Nino 4
Nino 3.4
Nino 3
Model
Obs
probability
°C
(b) Seasonal variances
Nino 4
Nino 3.4
Nino 3
(°C)²
Calendar month

Figure 6.

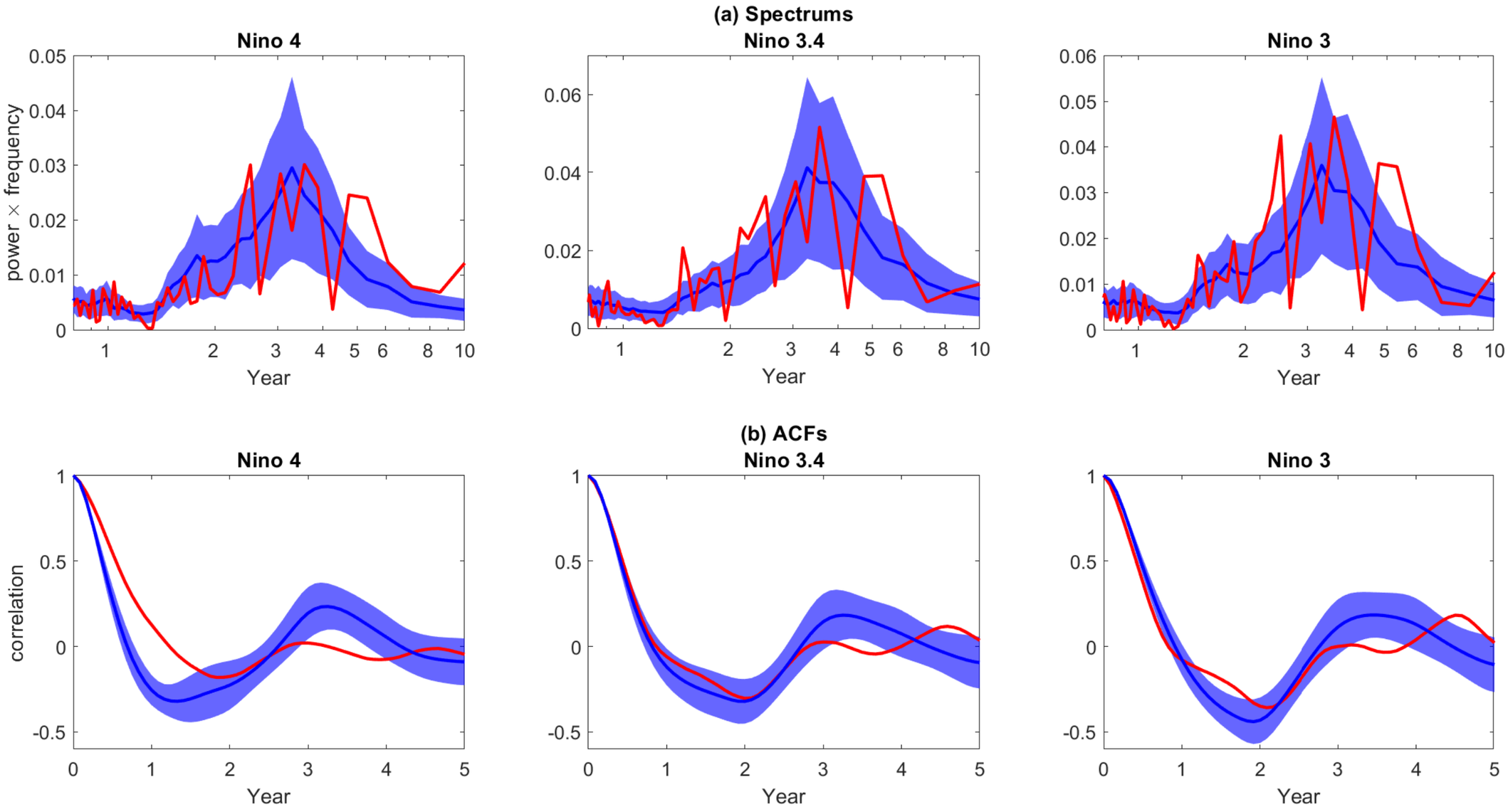
(a) Spectrums
Nino 4
Nino 3.4
Nino 3
power × frequency
Year
(b) ACFs
Nino 4
Nino 3.4
Nino 3
correlation
Year

Figure 7.

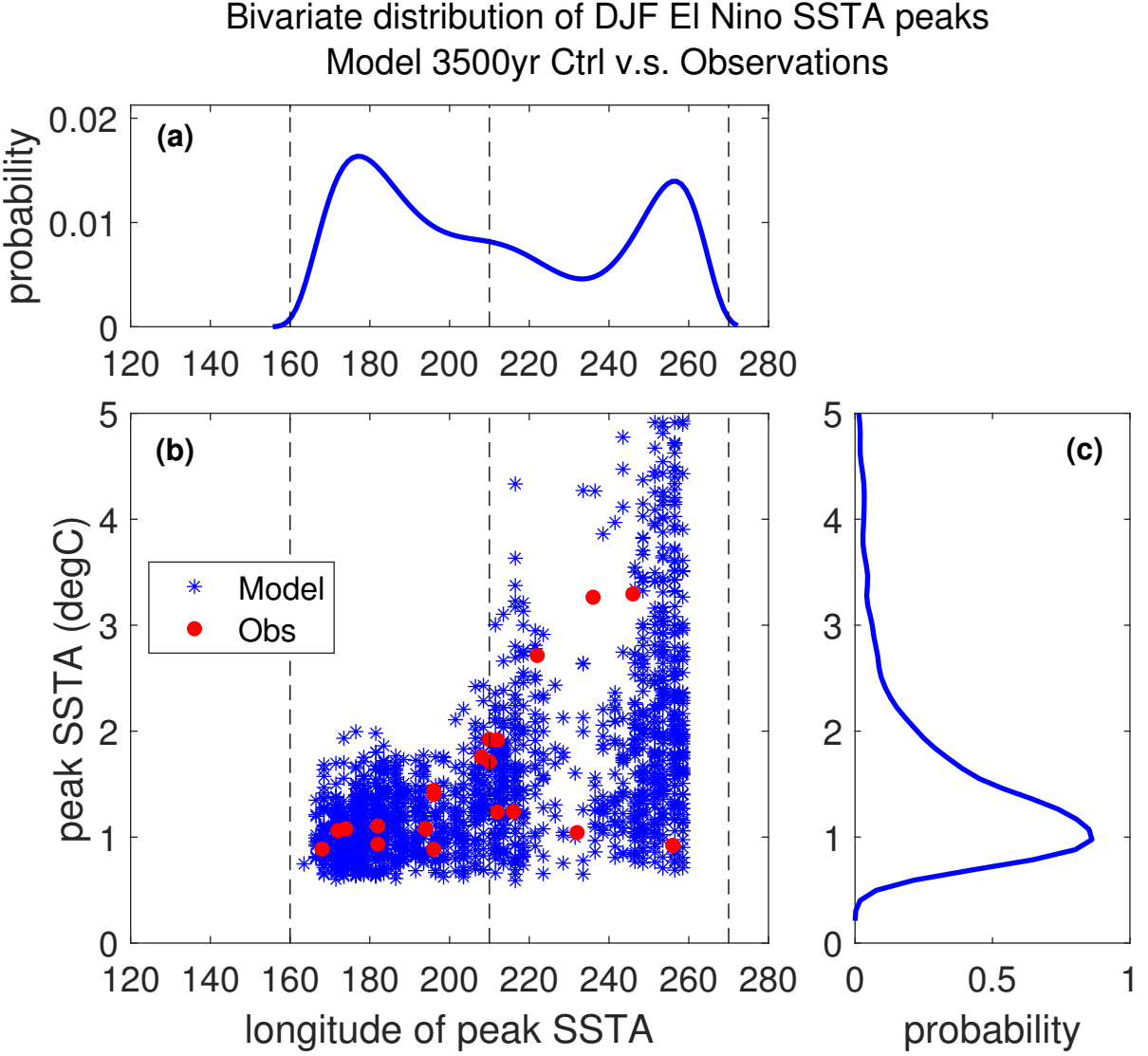
Bivariate distribution of DJF El Nino SSTA peaks
Model 3500yr Ctrl v.s. Observations
(a)
probability
0.02
0.01
0
120 140 160 180 200 220 240 260 280
(b)
Model
Obs
peak SSTA (degC)
5
4
3
2
1
0
120 140 160 180 200 220 240 260 280
longitude of peak SSTA
(c)
0
0.5
1
probability

Figure 8.

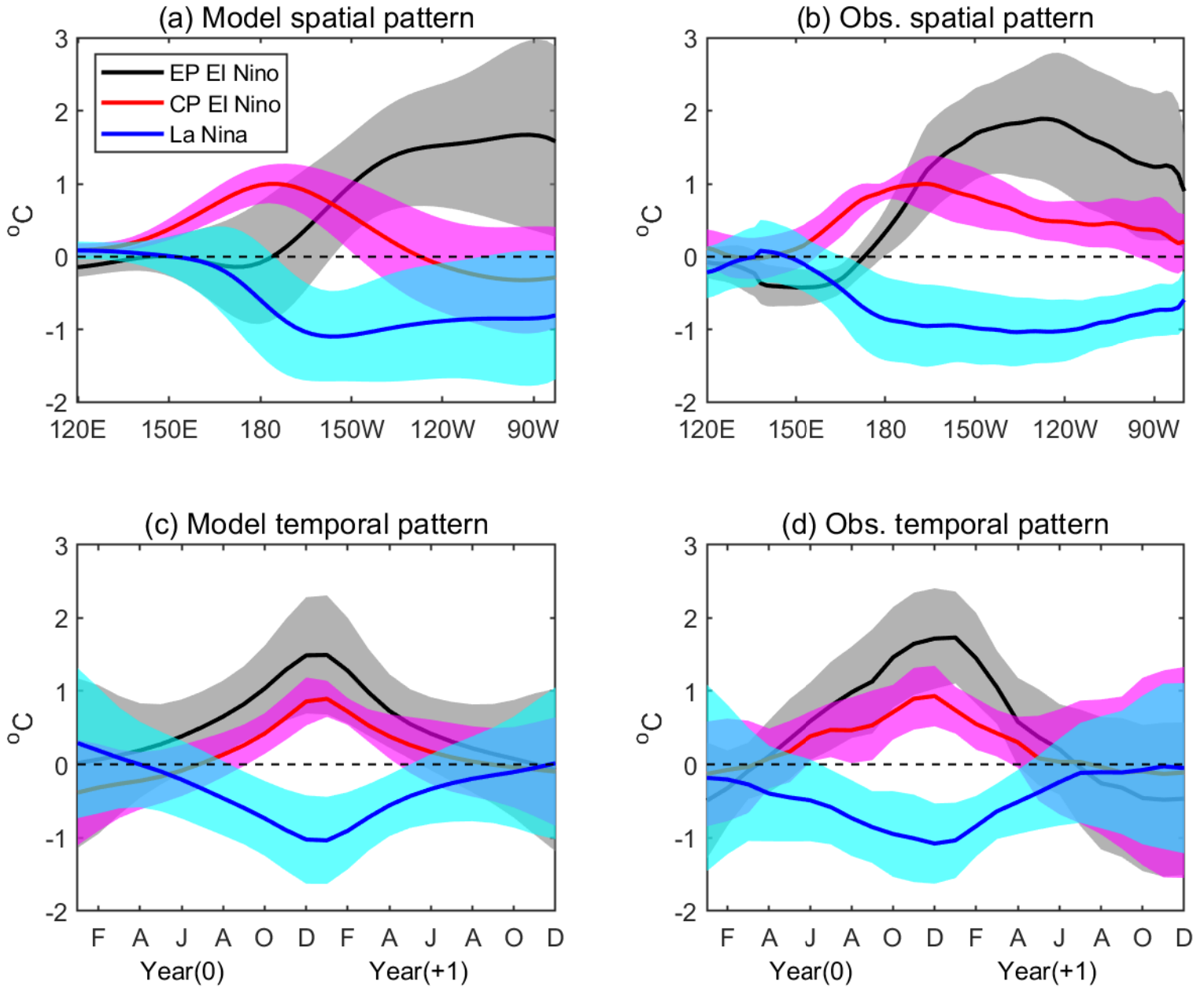
(a) Model spatial pattern
(b) Obs. spatial pattern
(c) Model temporal pattern
(d) Obs. temporal pattern
EP El Nino
CP El Nino
La Nina
°C
3
2
1
0
-1
-2
120E
150E
180
150W
120W
90W
F A J A O D F A J A O D
Year(0)
Year(+1)

Figure A1.

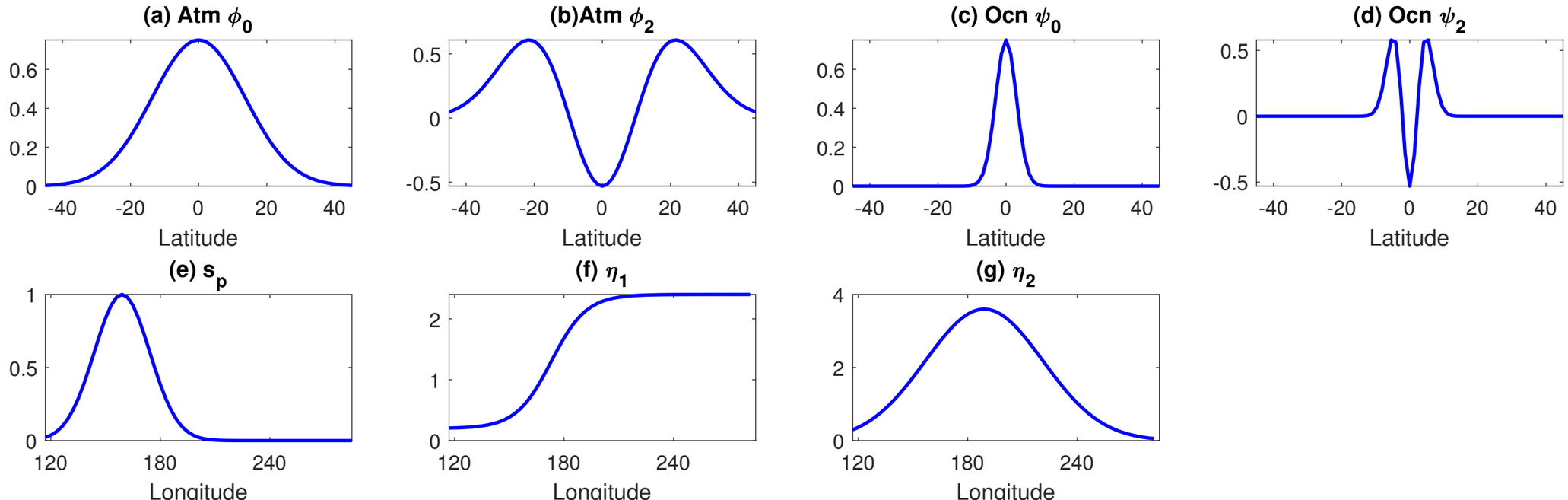
(a) Atm ϕ_0
0.6
0.4
0.2
0
-40
-20
0
20
40
Latitude
(b)Atm ϕ_2
0.5
0
-0.5
-40
-20
0
20
40
Latitude
(c) Ocn ψ_0
0.6
0.4
0.2
0
-40
-20
0
20
40
Latitude
(d) Ocn ψ_2
0.5
0
-0.5
-40
-20
0
20
40
Latitude
(e) s_p
1
0.5
0
120
180
240
Longitude
(f) η_1
2
1
0
120
180
240
Longitude
(g) η_2
4
2
0
120
180
240
Longitude

Figure B1.

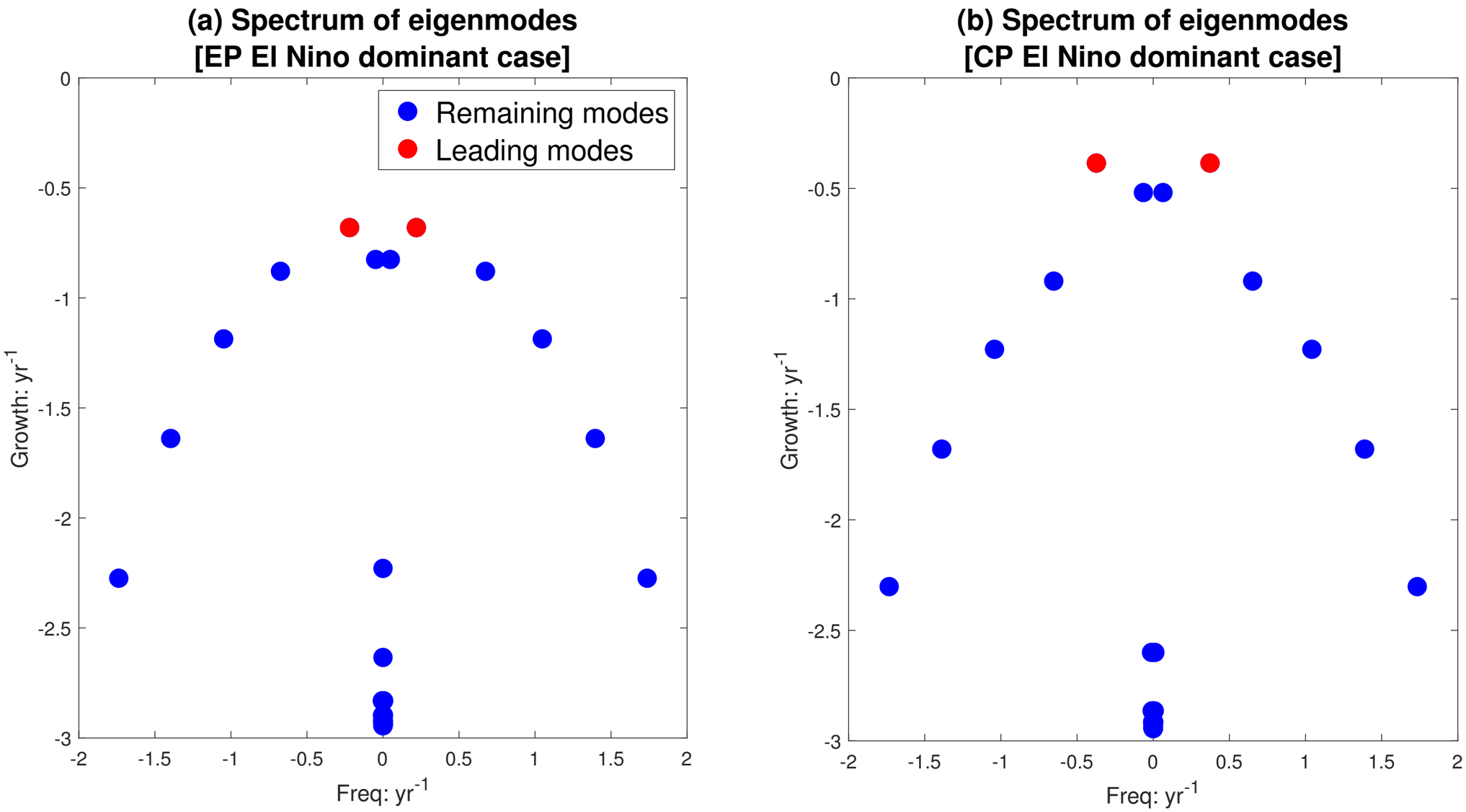
(a) Spectrum of eigenmodes
[EP El Nino dominant case]
Remaining modes
Leading modes
Growth: yr-1
Freq: yr-1
0
-0.5
-1
-1.5
-2
-2.5
-3
-2
-1.5
-1
-0.5
0
0.5
1
1.5
2
(b) Spectrum of eigenmodes
[CP El Nino dominant case]
Growth: yr-1
Freq: yr-1